**Board of Studies
in Chemistry**

PROJECT REPORT

**in part-fulfilment of the requirements
for the Degree of Master of Chemistry**

|	
Title	Spatially Resolved Reflectance Spectroscopy for Investigating Photon Migration and Depth Sensitivity in Turbid Media
Author	Jacob Morris
Date	May 2020

Contents

Abstract

This project investigates photon migration and depth sensitivity in turbid media through the application of spatially resolved reflectance spectroscopy. Building upon diffusion theory and historical photon transport models, including P1 approximations and boundary condition refinements, the study explores how light scattering and absorption govern subsurface reflectance behavior. Monte Carlo simulations, adapted from established methodologies, are employed alongside experimental measurements using fibre optic reflectance spectroscopy (FORS) to assess photon depth sensitivity and validate theoretical predictions. Varying concentrations of absorbers, simulated by layered ink samples, are used to characterize the relationship between reflectance spectra and optical density. Spectral Angle Mapping (SAM) is applied to quantify spectral similarities and evaluate subsurface contributions. The results demonstrate the utility of spatially resolved reflectance for probing internal structures of turbid materials, with implications for fields such as biomedical diagnostics and cultural heritage conservation. Future work is proposed to extend these models to time-resolved domains and more complex geometries for improved depth profiling and material characterisation.

Abbreviations glossary

SDS = Source-detector separation
FORS = Fibre optic reflectance spectroscopy
SAM = Spectral angle mapping

Introduction
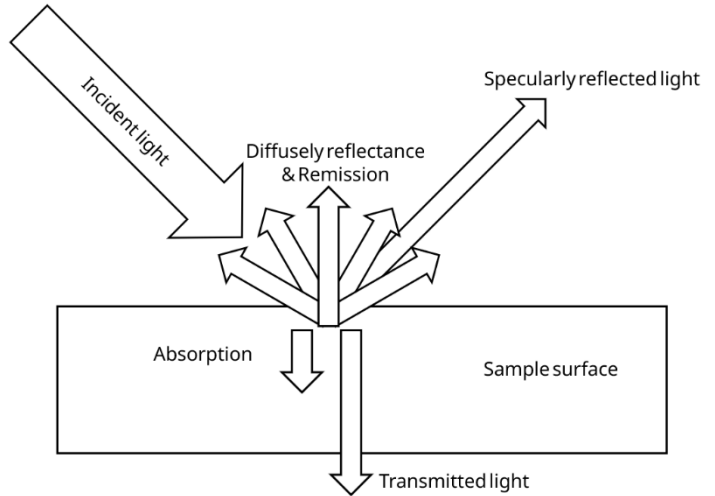
Figure 1: Schematic diagram of photon interactions at the surface of a turbid medium.

When electromagnetic radiation is incident upon a material, a number of interactions can occur at and below the surface, as illustrated in Figure 1. Incident light undergoes surface and subsurface interactions—primarily scattering, absorption, and reflection—whose dominance depends on the medium's optical properties. These govern the spatial distribution and spectral content of reflectance signals critical in diffuse and interactance spectroscopy. The proportion and nature of each interaction depend on the optical properties of the material, such as its absorption and scattering coefficients. Spectroscopy is the study of how matter interacts with electromagnetic radiation across a range of wavelengths. The specific wavelengths that a substance absorbs or emits are governed by its quantum mechanical structure of the system, as transitions between energy levels are discrete. These transitions obey selection rules that constrain allowable quantum changes—e.g., $\Delta l = \pm 1$ for dipole transitions—thereby shaping the spectral bands observed. Absorption can be classified by the resulting excitation: rotational (~0.1–10 cm^{-1}), vibrational (~100–4,000 cm^{-1}), or electronic (~10,000–50,000 cm^{-1}).[1]

Diffuse reflectance spectroscopy (DRS) measures the ratio of diffusely backscattered light to incident light across a spectrum of wavelengths. Each material exhibits a characteristic reflectance profile, determined by its absorption and scattering coefficients. Importantly, these interactions typically occur not only at the surface, but within a shallow subsurface region. Photons may undergo multiple scattering events before re-emerging or being absorbed, resulting in reflectance signals that are spatially offset from the point of incidence. Interactance spectroscopy extends this concept by resolving reflectance spatially—measuring light intensity as a function of source-detector separation. This spatial resolution enables the analysis of photon migration paths and provides depth-sensitive insight into the internal optical structure of turbid media. Although this project does not directly contribute to the development of diffusion theory, understanding these models provides essential context for interpreting reflectance behaviour and validating Monte Carlo simulations performed later in the study.

Diffusion Theory & Photon Migration
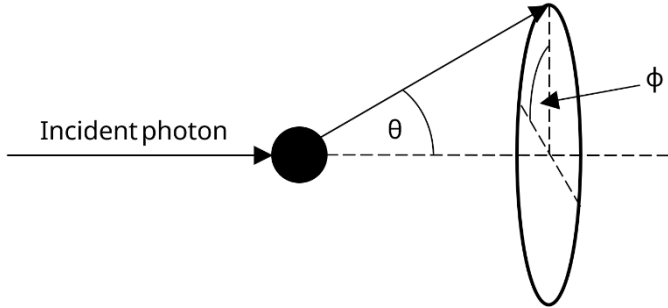
Figure 2: Schematic of photon scattering from an incident beam in a turbid medium. The scattering angle (θ) describes the deviation from the incoming direction. The azimuthal angle (φ) defines the rotation about the incident axis.

The directionality of subsurface scattering is characterised by the sample's anisotropy, quantified by the anisotropy factor g. This is defined as the mean cosine of the scattering angle (θ, see Figure 2), with values ranging from –1 (fully backward) to 1 (fully forward). When $g = 0$, scattering is isotropic, meaning photons are equally likely to scatter in all directions. Conversely, for $-1 \leq g < 0$, the scattering is backward-peaked with large directional changes, while for $0 < g \leq 1$, scattering is predominantly forward, with only small deviations from the incident direction.[2] This anisotropy is often accounted for by converting the scattering coefficient (μ_s, which describes the probability of scattering per unit length, cm^{-1}) to a reduced scattering coefficient (μ_s', cm^{-1}), using the relation ($\mu_s' = \mu_s(1 - g)$), which adjusts for directional bias.[2] This effectively removes the directionality bias and allows photon migration to be treated more diffusely in models. As discussed above, scattering and absorption predominantly occur near the material's surface layer, and their penetration is governed by the effective mean free path—the average distance a photon travels before a significant change in energy or direction occurs. In transport theory, this is defined as the reciprocal of the transport coefficient, which is the sum of the absorption coefficient (μ_a, cm^{-1}) and the reduced scattering coefficient (μ_s', cm^{-1}).

The photon migration problem in turbid media can be effectively approached using diffusion theory, which simplifies the radiative transport equation under the assumption that photon scattering dominates absorption. One of the earliest applications of this framework was by C. C. Johnson (1970)[4], who modelled light propagation in blood using isotropic scattering and derived an inhomogeneous Helmholtz equation to describe steady-state photon fluence. This laid the groundwork for analytical solutions to photon transport in biological tissue.

Alternative modelling approaches developed in the same era—such as multiple scattering field theory— offered mathematically rigorous treatments of photon migration, but were often too complex to apply to realistic, three-dimensional geometries. These models struggled with computational feasibility and generalisation, particularly in heterogeneous or layered media. To address these limitations, researchers turned to approximate solutions of the radiative transport equation. One such simplification was the P1

approximation, which expands the angular dependence of the radiative transport equation into a series of Legendre polynomials and retains only the first two terms. This reduced the problem to a tractable form while still capturing first-order anisotropy.[5] Building on this framework, Reynolds et al. (1976)[6] combined the diffusion approximation with the P1 approach to incorporate directional scattering into a modified Helmholtz equation, enabling analytical solutions under steady-state conditions in finite geometries.[5] Their model is governed by the equation:

$$[\nabla^2 - \frac{\Sigma_a}{D}]\rho_s(r,\theta,z) = -\frac{S(r,\theta,z)}{D}$$

where:

$\rho_s(r,\theta,z)$ is the scattered photon flux (W cm^{-2}), Σ_a is the macroscopic absorption cross section (cm^{-1}), D is the diffusion coefficient (transport constant)(cm), $S(r,\theta,z)$ is a generalised source term.This formulation allows analytical modelling of photon fluence that reflects the angular scattering characteristics of the medium—particularly useful for semi-infinite, anisotropic systems. The key innovation in their approach lies in the definition of the source term $S(r,\theta,z)$, which is split into isotropic and anisotropic components to reflect the angular dependence of scattering introduced by the P1 approximation:

$$S(r,\theta,z) = Q_0(r,\theta,z) - 3D\nabla \cdot Q_1(r,\theta,z)$$

where:

$Q_0(r,\theta,z)$ is the isotropic component of the source, $Q_1(r,\theta,z)$ is the anisotropic component of the source. In this formulation, the isotropic source term is given by:

$$Q_0(r,\theta,z) = q_0\Sigma_s e^{-\Sigma z}R(r)$$

where:

q_0 is the incident photon flux, Σ_s is the macroscopic scattering cross section (cm^{-1}), Σ is the total macroscopic cross section (absorption + scattering) (cm^{-1}), $R(r)$ is the radial source geometry profile. The anisotropic term $Q_1(r,\theta,z)$ follows a similar form but is scaled by the anisotropy factor g and aligned in the dominant direction of photon travel (typically the z-axis). This decomposition enables the model to account for forward-peaked scattering typical of biological tissues, bridging the gap between purely isotropic diffusion and more accurate representations of real-world light propagation.

The result of this formulation is a modified diffusion model that forms the theoretical foundation for subsequent analytical expressions—most notably, those used by Farrell *et al.* (1992)[17] to describe spatially resolved reflectance under steady-state conditions in semi-infinite media. Although this project does not extend diffusion theory directly, understanding its development—particularly through the P1 approximation—provides a foundation for reflectance modelling. This theoretical basis also contextualises the later use of Monte Carlo simulation and experimental interactance measurements to investigate photon depth sensitivity and optical behaviour in layered scattering media.

Historical Models & Key Papers

Groenhuis *et al.*

Groenhuis et al. (1983)[3] developed a diffusion model designed to better account for anisotropic scattering and boundary effects in semi-infinite turbid media. Unlike previous models that began with isotropic assumptions[7], their method applied transport theory using an anisotropic phase function—specifically a simplified Henyey-Greenstein function)[8] — to derive a diffusion equation that better captures anisotropic scattering and boundary effects. Their approach began with the radiative transfer equation, formulated in terms of spectral radiance $L(\boldsymbol{r}, \boldsymbol{s})$ (W m^{-2} sr^{-1} Hz^{-1}), and incorporated a general anisotropic scattering phase function $p(\boldsymbol{s}, \boldsymbol{s}')$ is the scattering phase function, describing the probability that photons travelling in direction $\boldsymbol{s}'$ are scattered into direction $\boldsymbol{s}$.

$$(\boldsymbol{s} \cdot \nabla_r) L(\boldsymbol{r}, \boldsymbol{s}) = -\rho \sigma_t L(\boldsymbol{r}, \boldsymbol{s}) + \frac{\rho \sigma_t}{4\pi} \int_{4\pi} p(\boldsymbol{s}, \boldsymbol{s}') \, L(\boldsymbol{r}, \boldsymbol{s}') d\omega'$$

where $\boldsymbol{s}$ is a unit vector, $\boldsymbol{r}$ is a point location, ρ is the particle number density (m^{-3}), σ_t is the total cross section (m^2), including both scattering and absorption and $d\omega'$ is the element solid angle (sr). By expanding the directional radiance in a Taylor series and incorporating the anisotropic phase function, they derived a modified diffusion equation involving the reduced scattering coefficient μ_s'. While the model assumes a homogeneous, semi-infinite medium, its treatment of anisotropic scattering and near-boundary behaviour makes it a suitable foundation for the Monte Carlo simulation presented in this project, which builds on the implementation from the original paper to estimate photon path depth in scattering media.

Keijzer et al.

Keijzer *et al.* (1989)[16] extended the diffusion model to handle multi-layered turbid media, such as biological tissues composed of stratified layers with different optical properties. Their approach retained the P1 approximation and introduced a custom boundary condition to account for anisotropic radiance, replacing the simpler image-source method used by Groenhuis *et al.*[3] They also implemented a finite element method (FEM) to numerically solve the diffusion equations across layered media, including interfaces with mismatched refractive indices. This enabled more accurate modelling of photon transport in stratified biological tissues, particularly where discontinuities in optical properties occur. However, the complexity of this layered model makes it less applicable to the homogeneous or semi-infinite scattering media considered in this project. Nonetheless, their treatment of boundary interactions forms an important part of the theoretical background for reflectance modelling in layered systems.

Farrell *et al.*

Farrell et al. (1992)[17] advanced reflectance modelling by combining the diffusion approximation with

an extrapolated boundary condition and validating their model against both Monte Carlo simulations and experimental data. They implemented the boundary condition proposed by Moulton et al.[18], which introduces a negative image source one mean free path above the extrapolated boundary, symmetrically positioned with respect to the real source within the medium. This method improved the modelling of photon escape near the surface, especially for mismatched refractive index boundaries. Using this boundary formulation and a simplified point-source assumption—in which all photons from a pencil beam are assumed to scatter at a single location, one mean free path below the surface—they derived an expression for spatially resolved diffuse reflectance:

$$R(\rho) = \frac{a'}{4\pi} \left[\frac{1}{\mu'_{tr}} \left(\mu_{eff} + \frac{1}{r_1} \right) \frac{e^{-\mu_{eff}r_1}}{r_1{}^2} + \left(\frac{1}{\mu'_{tr}} + 2z_b \right) \left(\mu_{eff} + \frac{1}{r_2} \right) \frac{e^{-\mu_{eff}r_2}}{r_2{}^2} \right]$$

where $\mu'_{tr} = \mu_a + \mu'_s$ is the transport coefficient (cm^{-1}), $a' = \mu'_s/\mu'_{tr}$ is the reduced albedo, $\mu_{eff} = \sqrt{3\mu_a\mu'_{tr}}$ is the effective attenuation coefficient, z_b is the extrapolated boundary height (cm), $r_1 = \sqrt{z_0{}^2 + \rho^2}$ is the distance from the detector to the actual photon source at depth z_0 and $r_2 = \sqrt{(z_0 + 2z_b)^2 + \rho^2}$, the distance from the detector to the image source placed above the extrapolated boundary. Here, ρ is the radial separation between the illumination and detection points on the surface (cm). This expression predicts reflectance as a function of source-detector separation and incorporates surface boundary effects, improving accuracy in layered or semi-infinite tissues.

They also derived an alternative version of this equation for an exponentially decaying source, representing a more physically accurate photon distribution. The two models were tested against Monte Carlo simulations for both index-matched and mismatched boundaries. Results showed that the single-scatter model performed better at shorter source-detector separations ($\rho > 0.5$ mean free paths), while the extended source model became more accurate at larger separations. Despite incorporating a more realistic photon distribution near the source, the extended source model consistently overestimated total reflectance. The authors attributed this to early photon escape before sufficient scattering, particularly near the surface. In addition to modelling, Farrell et al. compared two methods for estimating the internal reflection factor at mismatched boundaries — one from Groenhuis et al.[3] and one from Keijzer et al..[16] They found the Groenhuis-based method yielded better agreement with Monte Carlo simulations across a broader range of albedos but noted that neither method covered the full range of reduced albedos effectively.

They also explored an empirical reflectance expression of the form $R(\rho) = C_1\rho^{-m}e^{-C_2\rho}$, which provided a good fit over limited source-detector separation (SDS) ranges. However, its coefficients were dependent on the optical properties themselves, reducing its suitability for parameter extraction. This limitation motivated the development and validation of their analytical diffusion-based model.

Boundary Conditions & Geometry Considerations

The photon diffusion equation for an infinite medium is relatively simple and accurate. However, in practical applications such as interactance spectroscopy, measurements are typically conducted on semi-infinite geometries, where both the source and detector are positioned on the same surface and normal to the medium. In such setups, the geometry can significantly influence the model (See Figure 3), as the detected and illuminated regions depend on the optics and source-detector arrangement. For example, when a pencil beam is used, the illumination is often considered collimated or cylindrical, making the detected and illuminated regions match the physical apertures of the source and detector. Alternatively, if fibre optics or lenses are used, the geometry may be conical, and the effective detection and illumination areas depend on the numerical aperture and the working distance from the surface.
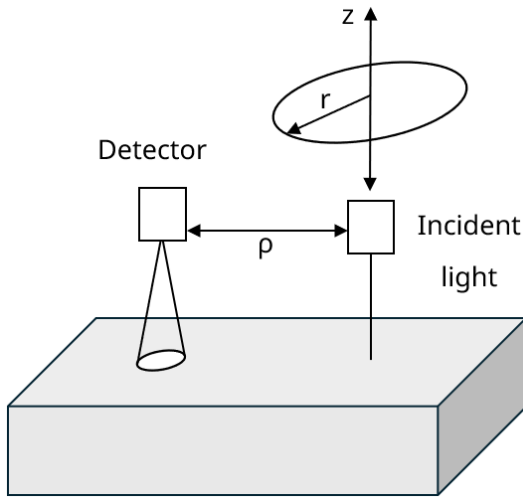

Figure 3: Measurement geometry in interactance spectroscopy for a semi-infinite turbid medium. A pencil beam (collimated source) delivers light normal to the surface, while detection occurs through a conical aperture defined by the optical collection geometry. The lateral source-detector separation (ρ) influences the depth sensitivity of the reflectance signal, with larger separations probing deeper regions of the sample.

Introducing a second medium (usually air) complicates the boundary, requiring the model to account for refraction, internal reflection, and the correct enforcement of boundary conditions. For instance, when light crosses the boundary from the medium to air, part of it reflects back internally, while the rest exits, leading to non-zero radiance beyond the surface. This boundary behaviour cannot be captured by simpler zero-flux assumptions and demands more accurate corrections.

In earlier models, such as Reynolds et al. (1976)[6], the problem was simplified using a mixed homogeneous boundary condition at the medium surfaces (e.g. $z = 0$ and $z = d$, the slab thickness). This condition approximates the boundary as:

$$\rho_s + f\boldsymbol{n} \cdot \nabla \rho_s = 0$$

where ρ_s is the scattered photon flux, f is a medium-dependent correction factor and $\boldsymbol{n}$ is the outward-facing normal vector. This zero-boundary flux condition neglects internal reflection and assumes all light reaching the surface exits the medium.

To model photon migration and reflectance, Reynolds et al. (1976)[6] assumed a cylindrical beam attenuated exponentially as $e^{-\Sigma z}$. They solved the corresponding diffusion equation using Green's

function methods, yielding a reflectance expression involving eigenfunction expansions and radial Bessel functions. While this approach offered an analytical solution for slab geometries, its accuracy was limited by the oversimplified boundary condition, which neglected internal reflection and assumed a zero-flux condition at the surface. While analytically elegant, the accuracy of this approach diminishes near the boundary due to the oversimplified flux condition, prompting later researchers to incorporate internal reflection and refractive index mismatch into boundary models.

Groenhuis *et al.* (1983) [3] later extended the zero-boundary condition by incorporating internal reflection (See Figure 4), improving boundary realism compared to earlier zero-flux approximations. Rather than assuming inward flux at the boundary is zero, they modelled it as a fraction of the outward flux:

$$\int_{2\pi,\mu>0} L_d(\boldsymbol{r},\boldsymbol{s})\,(\boldsymbol{s}\cdot\boldsymbol{z})d\omega = r_d \int_{2\pi,\mu>0} L_d(\boldsymbol{r},\boldsymbol{s})\,(\boldsymbol{s}\cdot\boldsymbol{z})d\omega$$

Here, $L_d(\boldsymbol{r},\boldsymbol{s})$ is the diffuse radiance, μ is the cosine of the angle between the photon direction and surface normal and r_d is calculated using Fresnel reflection and refractive index mismatch (approximated by Egan and Hilgeman[10]). This formulation introduced an improved expression for reflectance:

$$R(r) = \frac{1}{2\pi}\frac{(1-r_s)^2}{\pi r}\frac{dR_d(r)}{dr}$$

with:

$$R_d = \frac{8\rho\sigma_s'}{Dr_f{}^2}\sum_{n=1}^{\infty}\frac{\Gamma_n z_n R_n(r)}{(k_n{}^2 + \rho^2\sigma_{tr}{}^2)\lambda_i{}^2}$$

where r_f is the radius of the illuminated area, r_s is the specular reflection coefficient, $R_n(r)$ represents the radial Bessel-function solution, and z_n, Γ_n, k_n are components of the eigenfunction expansion derived by solving the diffusion equation with boundary conditions. These arise from the Green's function formulation used by Reynolds and extended by Groenhuis. λ_i refers to the radial scaling or effective beam radius, depending on the source geometry.
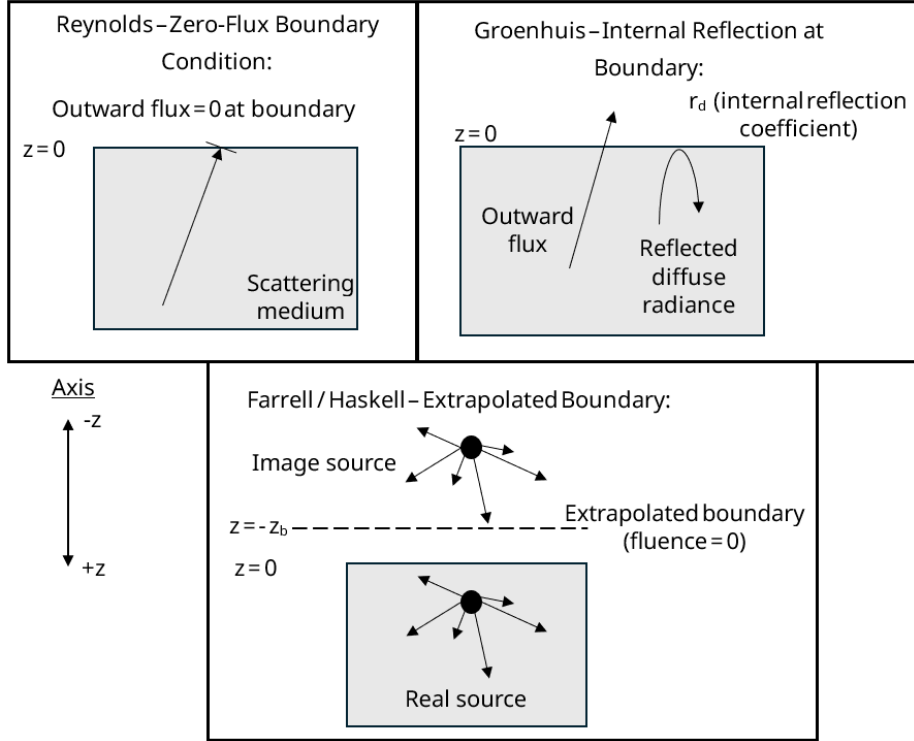
Figure 4: Comparison of boundary condition models in photon diffusion theory. (a) Reynolds et al.[9]: zero-flux boundary, no internal reflection — assumes all exiting photons leave the medium. (b) Groenhuis et al.[3]: includes partial internal reflection via reflection coefficient r_d, accounting for refractive index mismatch. (c) Farrell [17]/ Haskell[19]: applies an extrapolated boundary using a virtual source positioned at $z = -z_b$, improving accuracy near the surface.

These equations maintain similar functional forms to earlier models but now account for boundary mismatch. The zero-flux condition is only valid when the source-detector separation (SDS) is large compared to the transport mean free path, and the medium is much thicker than that path. These assumptions begin to fail at small SDS or in layered tissues, motivating the use of improved boundary corrections.

The extrapolated boundary condition was further refined by Farrell *et al.* (1992)[17], who introduced an image source located above the physical surface to enforce a zero-flux condition at a virtual boundary. This modification significantly improved agreement with experimental reflectance, especially near the surface. Haskell *et al.* (1994)[19] later formalised this approach, deriving the extrapolation length from transport theory and Fresnel laws. The virtual boundary shift depends on refractive index mismatch and offers a boundary model that accounts for refractive index mismatch and satisfies zero-flux conditions more effectively.

Kienle *et al.*[20] subsequently built on this by deriving closed-form solutions for steady-state and time-resolved diffusion in semi-infinite media, incorporating extrapolated boundaries and showing excellent predictive accuracy. Their models provided expressions for fluence and reflectance that could be directly fitted to data, enabling their use in diagnostic and imaging applications.

Together, these developments have shaped modern boundary modelling in optical spectroscopy, where the extrapolated boundary condition has become the standard for accurate photon migration modelling in turbid, semi-infinite media.

Monte Carlo Simulations vs Diffusion Models

Monte Carlo (MC) simulations are widely regarded as the most accurate method for modelling photon migration in turbid media due to their minimal reliance on assumptions. Unlike diffusion theory, which approximates photon transport under the condition that scattering dominates absorption, MC methods simulate the trajectories of individual photons, capturing their scattering and absorption events stochastically. This approach allows for accurate modelling of complex optical properties, geometries, and boundary behaviours, especially in cases where the diffusion approximation becomes unreliable. Diffusion theory tends to break down when the source-detector separation (SDS) is comparable to or smaller than the transport mean free path, as it assumes that photon paths are sufficiently randomized. At short SDS, photon migration remains highly directional and non-diffuse, violating the assumptions underpinning the diffusion model. MC simulations, by preserving the directionality and path history of each photon, accurately describe reflectance behaviour in these near-source regions.

In their two-part study, Farrell et al.[17] implemented both analytical diffusion models and MC simulations to compare reflectance predictions in media with matched and mismatched refractive index boundaries. The simulations launched a statistically large number of photons into a semi-infinite scattering medium and recorded the proportion returning to the surface at varying radial distances, generating a reflectance profile as a function of SDS. These results were compared against analytical predictions using both single-scatter and extended source models. Their findings showed strong agreement between the analytical and MC models at larger SDS, particularly when the extrapolated boundary condition was used. However, as SDS decreased, discrepancies became evident—specifically in mismatched boundary conditions—where the single-scatter analytical model aligned better with MC results than the extended source model. The overestimation of reflectance by the extended model was attributed to photon escape before undergoing sufficient scattering, an effect that diffusion theory cannot capture.

The second part of their study involved experimental validation using reflectance measurements from liquid phantoms. The analytical model was able to describe the data accurately under index-matched conditions, even at moderate SDS values. However, under index-mismatched conditions and shorter SDS, the MC simulations continued to outperform the diffusion model. These results emphasise the importance of boundary modelling and highlight the value of MC simulations for validating or calibrating analytical approaches.

In addition to validating diffusion-based models with MC simulations, Farrell et al.[17] also compared both approaches to an empirical reflectance function of the form:

$$R(\rho) = C_1 \rho^{-m} e^{-C_2 \rho}$$

where ρ is the radial source-detector separation, C_1 and C_2 are empirical fitting coefficients, and m is typically close to 2. This expression, adapted from earlier work by Groenhuis et al.(1983)[11], provides a convenient analytic form for fitting reflectance data. While the equation offered a good fit over specific SDS ranges, its primary limitation was that the fitting parameters were dependent on the optical properties of the medium. As a result, the expression could not reliably be inverted to extract meaningful absorption or scattering coefficients, as shown in Figure 5.
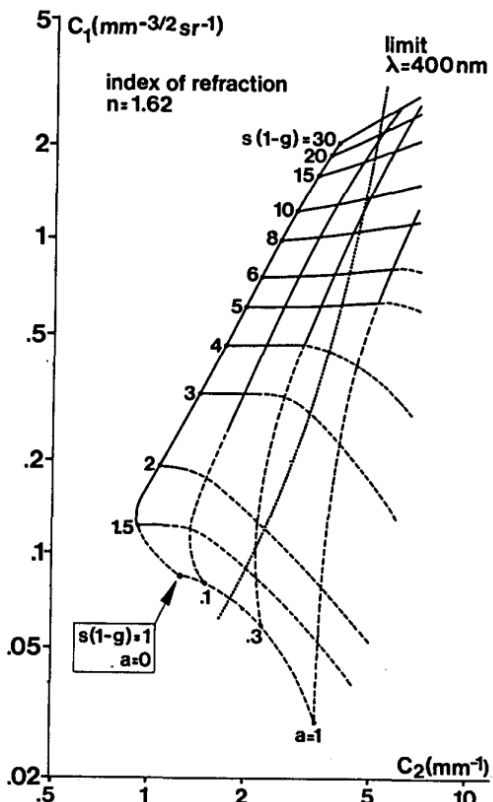
Figure 5: Comparison of spatially resolved reflectance predicted by Monte Carlo simulation, analytical diffusion models (single-scatter and extended source), and the empirical function $R(\rho) = C_1 \rho^{-m} e^{-C_2 \rho}$. The empirical model fits well over a narrow range of source-detector separations but fails to generalise, overestimating reflectance at large distances and mischaracterising near-surface behaviour.

The paper also compared their new method to the old calibration methods.[12, 13, 14, 15] Farrell et al. then evaluated how well this empirical model matched Monte Carlo reflectance profiles across a range of optical properties and boundary conditions. Although the empirical function visually aligned with MC predictions over narrow SDS intervals, it systematically overestimated reflectance at larger separations and failed to capture near-surface behaviour—particularly under index-mismatched conditions. In contrast, the diffusion model, especially when incorporating the extrapolated boundary condition, produced reflectance predictions that more closely matched Monte Carlo results across the full SDS range. These findings reinforced the inadequacy of empirical forms for quantitative analysis, particularly in the presence of refractive index mismatch or layered geometry.

In the context of this project, which aims to estimate photon path depth and understand subsurface contributions to reflectance using both spectral measurements and Monte Carlo simulation, the use of physically derived models is essential. The limitations of empirical fitting further justify the application of diffusion theory and MC simulation as robust tools for interpreting reflectance behaviour in scattering media.

Discussion & Future Work

Beyond biomedical applications, interactance spectroscopy has found increasing utility in the field of cultural heritage. Hyperspectral imaging techniques, which rely on spatially resolved reflectance principles, allow conservators to non-invasively probe beneath pigment layers. This enables detailed material mapping of historic artworks, supporting authentication, conservation strategy, and reconstruction of underdrawings. These depth-sensitive techniques illustrate how optical modelling of photon migration can reveal previously inaccessible structural information in layered organic materials.[21, 22]

This review has outlined the theoretical and computational foundations for modelling reflectance in turbid media, focusing on photon migration, boundary conditions, and source-detector geometry. The evolution from classical diffusion theory to more advanced models—including the P1 approximation and the extrapolated boundary condition—has significantly improved the accuracy of reflectance predictions. However, diffusion theory remains limited at small source-detector separations (SDS) and near refractive index boundaries, where the assumption of diffuse transport breaks down. Monte Carlo (MC) simulations, by tracking individual photon trajectories, overcome these limitations and serve as a gold standard for validating analytical models.

While this project does not aim to extend diffusion theory itself, the framework serves as a useful baseline for evaluating photon migration in layered scattering media. A modified Monte Carlo code, adapted from Groenhuis et al.[3], has been developed to estimate mean penetration depth as a function of SDS. These simulations complement experimental interactance measurements using milk-based phantoms, both with and without embedded absorbers, to assess how depth and optical heterogeneity affect spatially resolved reflectance.

In parallel, spectral angle mapping is employed to identify spectral similarities in reflectance data, providing a method for pigment matching that is sensitive to subsurface signal contributions. This dual approach—modelling physical light transport while analysing spectral content—allows the project to

probe both spatial and spectral sensitivity of the system and assess its reliability for pigment classification or subsurface detection.

Future work could involve extending these models to time-resolved reflectance using pulsed light sources or exploring more complex geometries that better replicate real-world applications. Further validation of depth-resolved predictions, especially through experiments with layered absorbers of known composition and thickness, would enhance confidence in the simulation outputs. Overall, by combining diffusion theory, Monte Carlo simulation, and experimental spectroscopy, this project contributes to the broader effort of quantitatively interpreting subsurface reflectance in turbid media—a goal relevant to fields ranging from biomedical diagnostics to art conservation.

Aims

The primary aim of this project is to investigate photon migration and depth sensitivity in turbid media using spatially resolved reflectance spectroscopy. Specifically, the project seeks to:

- Understand and review theoretical models of photon transport, including diffusion theory and boundary condition refinements.
- Develop and implement Monte Carlo simulations to model photon paths and assess mean penetration depths as a function of source-detector separation.
- Experimentally measure spatially resolved reflectance spectra from layered ink samples using fibre optic reflectance spectroscopy (FORS).
- Analyse how absorber concentration influences reflectance spectra, and evaluate spectral shape consistency through Spectral Angle Mapping (SAM).
- Compare experimental results to simulated data to validate theoretical predictions of photon migration and depth sensitivity.
- Explore the potential applications of depth-resolved reflectance measurements for material characterisation in fields such as biomedical imaging and cultural heritage conservation.

Results and discussion

Reflectance spectroscopy

Concentration of absorber and reflectance

For the reflectance part of this project for completeness we aimed to replicate similar results to Norris (2005)[24] by investigating how the log(1 / R) spectra would change with changing concentration of absorber. In that paper Norris preached about the utility of this approach in correlating spectral intensity with concentration despite variations in sample. The easiest way to investigate this was to simply paint a varying number of layers of ink onto paper. A possible inconsistency predicted during the qualitative creation of the gall ink samples was the inconsistent spread of ink within each layer this was attempted to be solved by the measurement of three different spots of each sample and averaging them. These results are displayed in Figure 6.
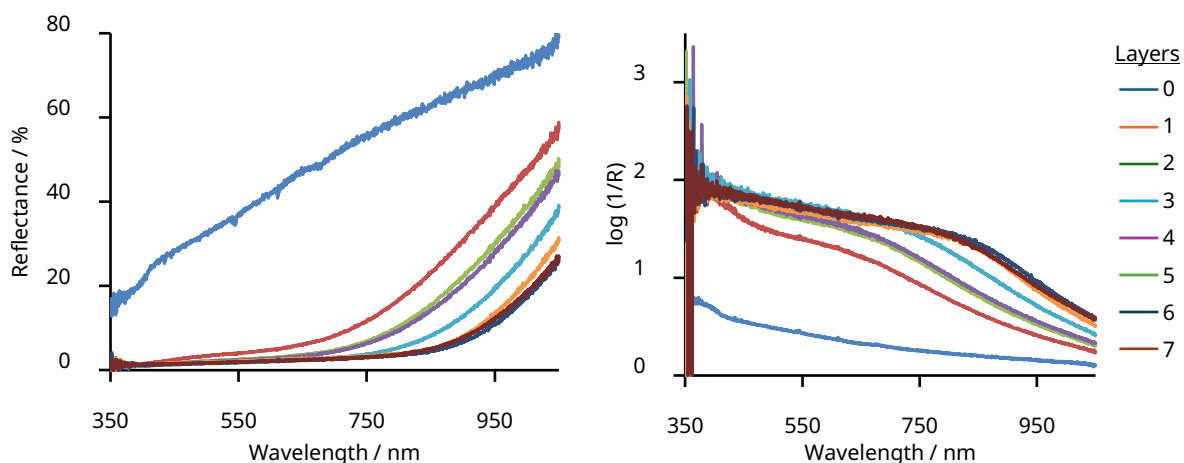

Figure 6: The average percentage reflectance and log (1 / R) spectra obtained from the average of three reflectance spectra of different incidence spots of the sample. The sample varies by the number of layers of ink .

The data followed the anticipated trend of decreasing reflectance and increasing log(1 / R) with additional ink layers, reflecting higher optical density. This pattern is consistent with findings by Norris (2005).[24] The spectral shape remaining broadly consistent further supports its reliability as an interpretive tool in this context. A minor deviation from this expected result is the comparison of 6 and 7 layers. This could be due to multiple factors such as the spectrometer having less sensitivity and a greater noise to signal ratio for highly absorbing samples. Another possible reason is that as discussed previously the distribution of ink may not have been even across each level and the area of layer six that a seventh layer was added to may have had a greater concentration than that of the area of layer six that was used for the six layer measurement. Since these results were average reflectance spectra (of three different incident

spots) a standard deviation of each line change at each point could be calculated, these results are shown in Figure 7. This showed that the two lines were approximately within one standard deviation of each other which can be explained by the uneven distribution of ink. The uncertainty and inconsistency in these results are expected to be larger than a standard deviation as the sample size (the three spots) is very small.
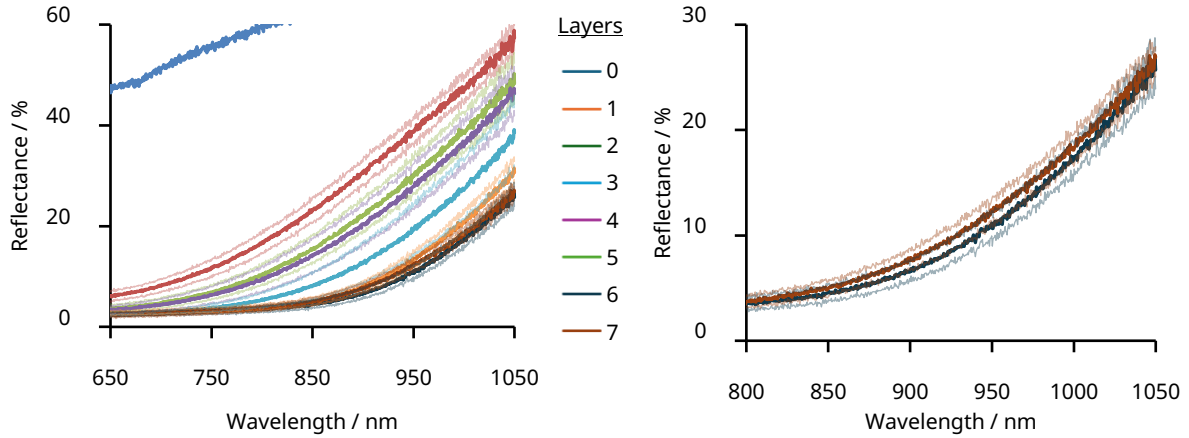

Figure 7: Average % reflectance data for varying numbers of layers of ink with the faint lines being plus and minus one standard deviation from the average values. On the right is the zoomed in spectra of six and seven layers.

After this a Fiber Optic Reflectance Spectroscopy (FORS) probe was conducted on the samples to acquire a reflectance spectra over a wider range of wavelengths (400 - 2500 nm). It does this by recording 2 spectra simultaneously one in the visible region and one in the near infrared (NIR) and infrared (IR) region then uses a program to align the spectra. The output is the two different spectra and when the overlapping wavelengths are removed it can lead to a discrepancy at ~940 cm^{-1} if the instrument is not focused or the references set properly.
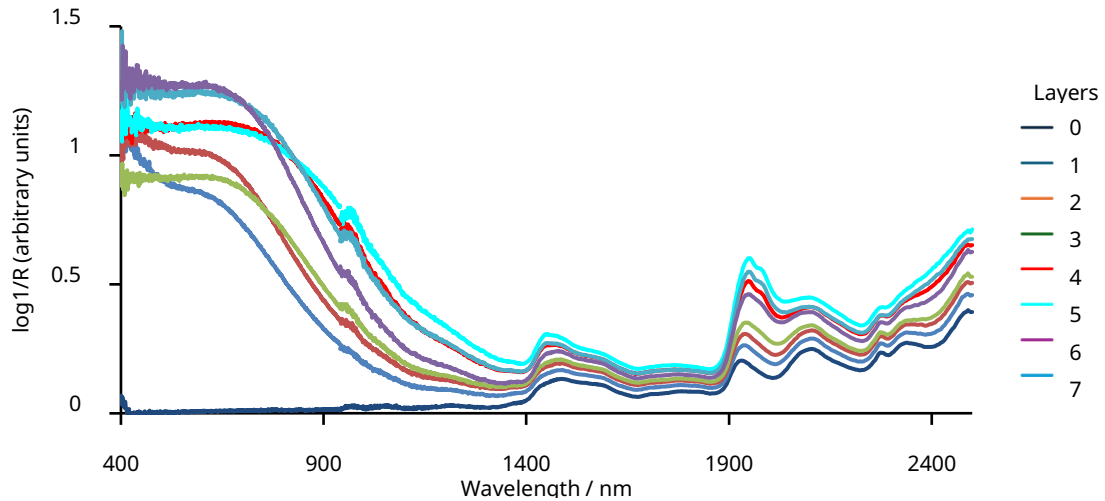

Figure 8: Log(1 / R) spectra of samples with varying numbers of ink layers (0–7), measured using a Fiber Optic Reflectance Spectroscopy (FORS) probe across the 400–2500 nm range. Increased layering generally leads to higher optical density and lower reflectance, shifting the log(1 / R) curves upward.

17

The FORS measurements revealed how the reflectance spectra changed with increasing numbers of ink layers (Figure 8). As additional layers are applied, the optical density should increase, causing a uniform upward shift of the log(1 / R) spectra while maintaining the same overall spectral shape. However, the results show that while there is a general trend toward increased log(1 / R) with more layers, the spectra are not simple vertical translations of one another. Instead, there are changes in curvature and spectral features, particularly in the 900–1400 nm region. These discrepancies could arise from uneven application of the ink layers, slight variations in sample surface roughness, or instrumental alignment issues between the visible and infrared regions, particularly around the overlap region (~940nm). Such factors can introduce spectral artifacts and small distortions that deviate from ideal behaviour.
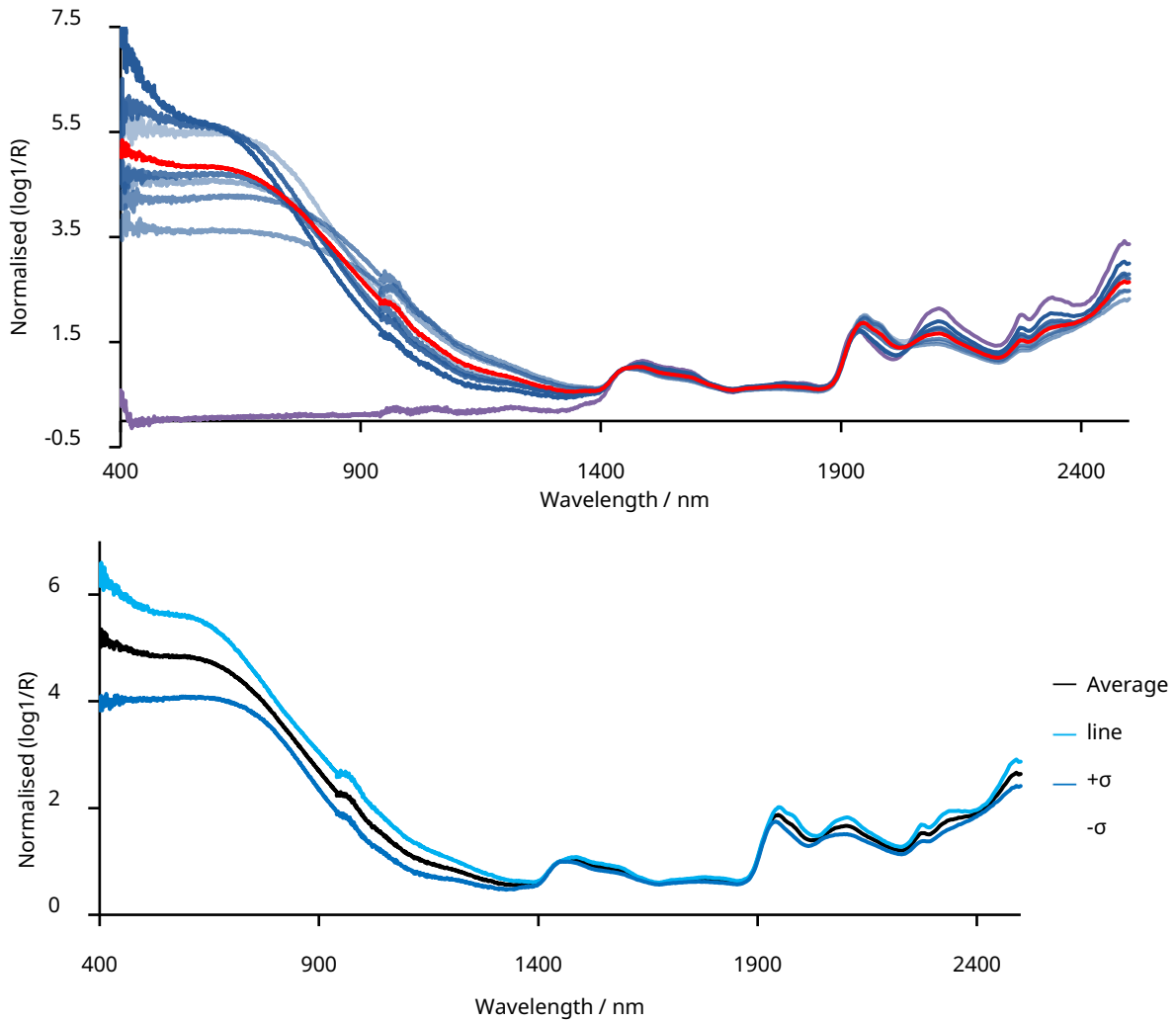
Figure 9: Top: Normalised log(1 / R) spectra of ink samples with varying numbers of layers. Each individual spectrum has been normalised to allow for direct comparison of spectral line shapes regardless of absolute reflectance. The red line represents the average spectral shape across all samples. Bottom: The average normalised line shape with bands indicating plus and minus one standard deviation (σ) at each wavelength highlighting the degree of variability across the line shapes.

To better compare the spectral line shapes independently of absolute intensity, the log(1 / R) spectra were normalised and plotted together (Figure 9). In the top plot, although the overall trends are broadly similar, there are clear deviations between the individual spectra, particularly in the 400–900 nm region and near 1400 nm. Ideally, if only the optical density varied between samples, the normalised line shapes would be exactly the same and fully overlap. However, the spread of the data suggests that additional factors—such as inconsistencies in ink layering, sample surface variation, or instrumental artefacts—are affecting the measurements. The red line shows the average normalised spectrum, providing a reference for the mean spectral shape. The bottom plot isolates this average line and overlays ±1 standard deviation (σ) bands, which quantify the extent of sample-to-sample variability. Notably, larger deviations occur in regions of stronger absorption, indicating that measurement conditions or sample heterogeneity may influence the spectral features more strongly there.

This variability was an unexpected result. It was initially assumed that differences between spectra would mainly be vertical shifts (differing magnitudes of bands), corresponding to increased optical density. A major factor considered from qualitative observation of the sample and from the large log(1 / R) values was that the samples may have been too strongly absorbing leading to an increased error from noise and layer application. To address this, a second set of samples with much thinner ink layers was prepared, aiming to maintain a more linear relationship between absorption and reflectance. For the analysis of these spectra a more sophisticated comparison technique—Spectral Angle Mapping (SAM)—was employed to quantitatively assess the similarity between spectral shapes.

Spectral Angle Mapping (SAM) is a commonly used method for comparing spectra, particularly in remote sensing and hyperspectral imaging.[23] Rather than comparing absolute reflectance values, SAM treats each spectrum as a vector in n-dimensional space (where n is the number of wavelength bands) and calculates the angle between these vectors. Smaller angles correspond to more similar spectral shapes, independent of overall intensity. This technique, originally described by Kruse et al. (1993)[23], has the advantage of being robust against differences in intensity, making it highly appropriate for assessing line shapes that are expected to be very similar but at different magnitudes like log(1 / R) data of varying concentration of absorber.

The spectral angle mapping (SAM) equation was then used to compare the spectral line shapes:

$$SAM\ score = cos^{-1}\left(\frac{\sum_{i=1}^{n} Spec\ 1_i\ Spec\ 2_i}{\sqrt{\left(\sum_{i=1}^{n} Spec\ 1_i{}^2\right)}\sqrt{\left(\sum_{i=1}^{n} Spec\ 2_i{}^2\right)}}\right)$$

where, n = the number of bands and Spec 1 and 2 = the intensities at that band.[23]
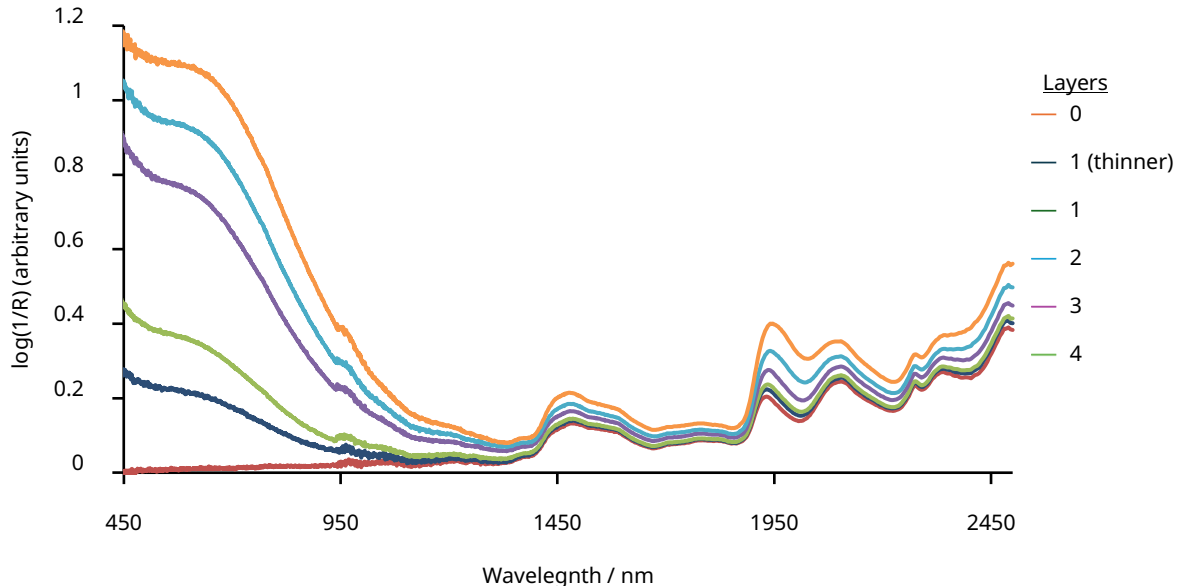

Figure 10: Log(1 / R) spectra for samples with varying numbers of ink layers measured across the 450–2500 nm range. Each spectrum shown is the average of measurements taken at three different spots across each sample to reduce the impact of uneven ink distribution from manual painting. The "1 (thinner)" sample was painted with a qualitatively thinner application of ink compared to the other samples.

Figure 10 show the expected result that increasing the number of layers generally leads to higher log(1 / R) values, corresponding to greater optical density. The overall spectral shapes remain broadly consistent, indicating that absorption primarily scales the spectra without introducing significant distortions under these thinner-layer conditions.

Table 1: Spectral Angle Mapping (SAM) scores (in degrees) comparing normalised log(1 / R) spectra between samples with different numbers of ink layers. Smaller angles correspond to greater spectral similarity.

	1 (thinner)	1	2	3	4
1 (thinner)	0	9.2	17.6	19.0	20.4
1	9.2	0	9.2	11.2	13.5
2	17.6	9.2	0	2.6	5.6
3	19.0	11.2	2.6	0	3.2
4	20.4	13.5	5.6	3.2	0

The SAM scores presented in Table 1 quantify the similarity between the normalised spectral shapes of the different ink layers. The largest spectral difference occurs between the thinnest sample ("1 (thinner)") and the sample with four full layers, yielding a SAM score of 20.4°. This

trend is consistent with increasing optical density: as the number of layers increases, the SAM score relative to thinner samples decreases. A possible reason for the larger spectral differences at lower layer numbers is that the samples are further from being optically thick, allowing the underlying paper substrate to contribute to the measured reflectance. As a result, the spectra at low ink coverage may represent a mixture of the paper and ink signatures, leading to altered spectral features. To avoid the problem of light passing through the entire sample and being reflected back by the stage underneath the sample, since a thin layer of ink on paper is not very optically thick, the samples were suspended during the measurements. Once sufficient ink is applied to achieve optical thickness, the spectra become increasingly dominated by the ink itself, resulting in lower spectral angle differences. Finally, these results suggest that achieving optical thickness without very high absorption is critical for obtaining pure sample spectral signatures in reflectance spectroscopy. Thin or uneven layers introduce variability not only in intensity but also in spectral shape, which can complicate compositional or classification analyses.

Pigment analysis

For the known pigment analysis 32 samples were made from 32 different pigments of historical importance, some being the same type of pigment but from different brands, for example L. Cornelissen & Son (Corn.) and Kremer Pigmente (Krem.). Each sample was made of a mixture of finely ground sodium chloride and pigment in the ratio of 2:1. Initially the reflectance spectra were recorded in the visible and near infrared region (VNIR) and converted to log (1/R) spectra (Figure 11).
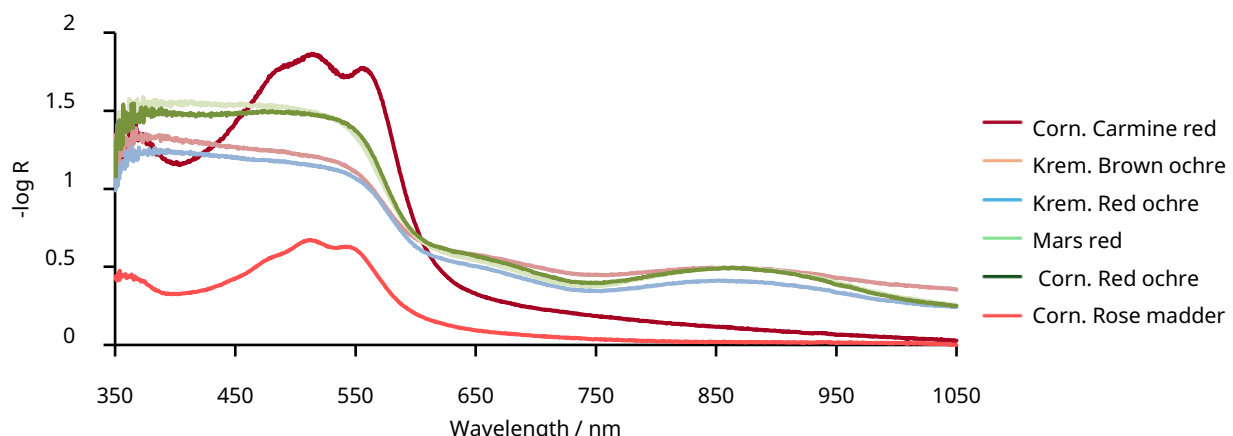

Figure 11: Example log(1 / R) spectra for six red-coloured pigment samples from the set of 32 historical pigments. Reflectance measurements were recorded over the visible and near-infrared (VNIR) range (350–1050 nm) and transformed to log(1 / R) to enhance spectral feature visibility.

Table 2: Some example data from SAM comparisons of pigments.

Pigment 1	Pigment 2	SAM score / ° (3sf)
Kremer Pigmente Red ochre	L. Cornelissen & Son: Red ochre	2.52
Mars red	L. Cornelissen & Son: Red ochre	1.93
Kremer Pigmente Yellow ochre	L. Cornelissen & Son: Yellow ochre	5.99
L. Cornelissen & Son: Verdigris	L. Cornelissen & Son: Rose madder	68.1
L. Cornelissen & Son: Antwerp blue	L. Cornelissen & Son: Yellow ochre	56.9
$MgCO_3$	Kaolinite	124
L. Cornelissen & Son: Rose madder	L. Cornelissen & Son: Carmine red	6.68
L. Cornelissen & Son: Azurite	L. Cornelissen & Son: Blue verditer	5.18

The differences in spectral shape and intensity between pigments in Figure 11 highlight the variation in optical properties, even among pigments of similar colour appearance. The SAM score comparison was applied to some of the combinations of pigments, some of these results can be found in Table 1. As expected, there were low values for pigments of the same compound from different companies but not exactly 0 degrees difference. This can be explained by differences in the production process and by many of these pigments being derived from naturally occurring mixtures of chemicals thus different quantities of chemicals making them. Also as expected comparing two very different spectra such as verdigris and rose madder results in very large SAM scores. In addition to the expected trends, some interesting results were observed. The comparison involving kaolinite and $MgCO_3$ produced exceptionally high SAM scores. This can be attributed to multiple factors such as their lines having different weakly absorbing spectral features. These materials have very low absorption across most of the measured spectral range, meaning that the absolute differences between spectra were small and can be dominated by random noise. Since the SAM algorithm operates on the vector shape rather than absolute magnitude, even small amounts of measurement noise can result in large angular separations when the overall signal strength is weak. And finally, the $MgCO_3$ was so weakly absorbing that for sections of its spectra its reflectance is more strong than the reference tile, this is likely due to the high purity of sample and the chance of the reference tile being very minorly dirty/stained from its handling and use over time.

The analysis of these pigments led to a discovery for the pigment samples labelled as "Blue Verditer" by Cornelissen & Son and by Kremer Pigmente and "Blue Bice" by Kremer Pigmente as they had an unusually small SAM score when compared to azurite samples. For example, there SAM scores when compared to "Azurite" by Cornelissen & Son were: 1.5° "Blue Bice" by Kremer Pigmente, 2.3° "Blue Verditer" by Kremer Pigmente and 5.2° "Blue Verditer" by Cornelissen & Son. Upon further investigation, it was found that these pigments are a synthetic

forms of azurite so all contain the compound $Cu_3(CO_3)_2(OH)_2$.[25, 26, 27] These connections were not previously known prior to the spectral and SAM analysis, demonstrating how reflectance spectroscopy can reveal information about pigment composition and manufacturing methods.

Similarly, a close spectral similarity was observed between Rose Madder and Carmine Red, with a low SAM score despite originating from historically distinct sources. Further research revealed that both pigments are based on very similar anthraquinone-based molecular structures[28,29], again highlighting how spectral analysis can provide insight into underlying chemical similarities even when this information was not initially available (see Figure 12). These results illustrate the broader utility of reflectance spectroscopy and spectral angle mapping not only for pigment identification but also for inferring chemical relationships between materials.
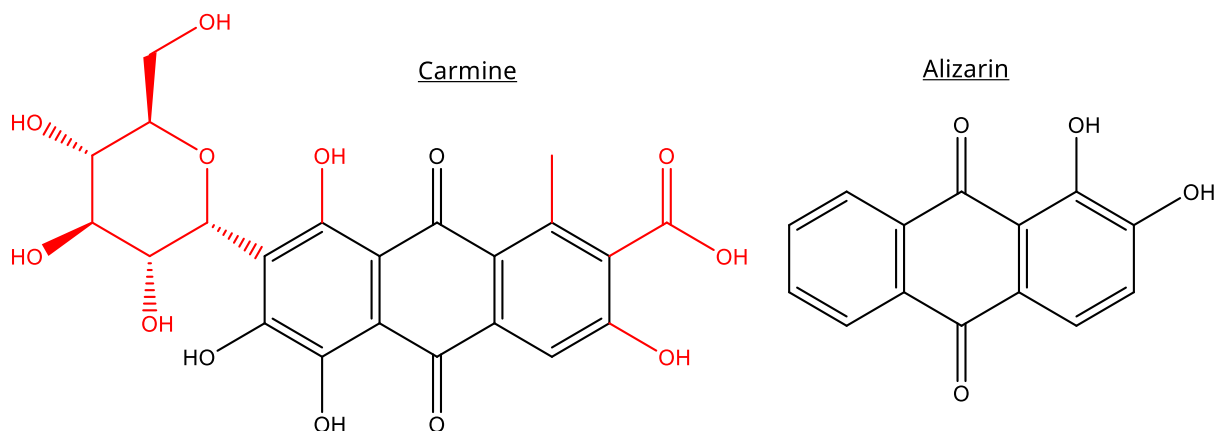

Figure 12: Chemical structures of Carmine (left) and Alizarin (right), the primary colouring agents in Carmine Red and Rose Madder pigments, respectively. Both molecules are based on anthraquinone frameworks, with Carmine consisting of a glycosylated anthraquinone derivative (carminic acid) and Alizarin being a simple dihydroxyanthraquinone. Their structural similarities help explain the observed spectral similarities in reflectance spectroscopy measurements. [28,29]

The spectral range of interrogation was then increased by measuring the FORS spectra for the 32 pigments. It was of interest to see how similar the two spectra from the two different measurement instruments were for the same pigment, so SAM scores were calculated for each pigment. To do this both spectra needed to be interpolated across the range of wavelength that overlap, this is due to SAM requiring the two spectral intensities being inputted at a time must be of the same band and the two recorded spectra swept across different wavelengths with different step sizes. The one-dimensional interpolation was conducted using 0.01 nm spacing, this is relatively small compared to the data spacing ~0.47 nm for the visible only spectra and ~0.48 in the visible region and ~5 nm in the IR region. The use of small interpolation wavelength step results in the capture of the detailed spectra shape, if relatively large steps were

used spectral features could be missed.

Table 3: Selected pigments and their corresponding Spectral Angle Mapper (SAM) scores (°) comparing visible and FORS spectra following interpolation. A lower SAM score indicates a closer match to the reference spectrum. Full list of pigments and values is provided in the Appendix.

Pigment	Krem. Blue bice	Corn. Terre verte	Mars red	Zinc white	$MgCO_3$
SAM score (°) (2sf)	0.97	1.20	2.48	44.63	96.38

These results showed very good overall agreement with the same issues previously seen of very weakly absorbing samples having higher SAM values, likely for the same reason of very small intensities and some negative intensities. As before out of the white pigments $MgCO_3$ has the highest values, is least similar.
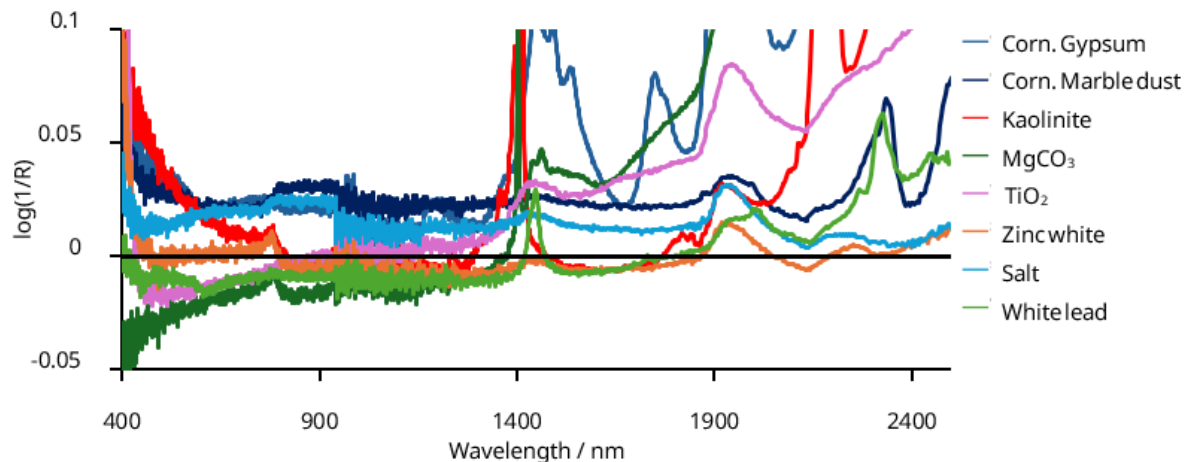
Figure 13: A zoomed in plot of the FORS measurements of the white coloured pigments. Showing how multiple of them are more reflective than the reference at some wavelengths.

These results suggest that the samples are more strongly reflective than the reference used, which should not be possible. This emphasizes the need to set or record accurate references especially for very weakly absorbing samples as they cannot be compared using the SAM approach if their $\log(1 / R)$ values are negative. Now that a spectral library has been recorded and a spectral comparison method proven to be accurate for non-weakly absorbing samples, it has been applied to try to identify and compare spectra of other coloured samples.

Applying the spectral library

A mock manuscript was investigated by recording spectra of different antique pigments used to make it and compared to similar coloured pigments from the library.

24

Table 4: A table of SAM values calculated by comparing chosen pigments from the spectral library with mock manuscript pigments.

Library pigment	Manuscript pigment	SAM score /° (1dp)	Manuscript–paper SAM /° (1dp)	Feature range / nm	SAM score of features /° (1dp)
Corn. Red ochre	Red ochre1	9.7		400-1100	8.1
	Red ochre2	10.5			8.1
Corn. Carmine red	Red lead	19.4		400-900	19.3
Corn. Yellow ochre	Orpiment	14.5		400-1320, 1840-2045	14.1
Krem. Yellow ochre		18.5		400-1320	17.7
Krem. Fib malachite	Malachite1	1.6		400-1500, 2125-2500	1.5
	Malachite2	8.8			8.2
Corn. Blue verditer	Azuite1	8.3	6.1	400-1101, 2170-2500	3.6
	Azuite or Lazurite	23.1	22.7		22.6
	Azuite2	8.6	6.0		5.1
	Azurite3	22.0	10.2		8.4
Corn. Azurite		21.2	9.2		8.3
Corn. Lapiz L	Azuite or Lazurite	7.7		400-930	6.9
	Lapis Lazuli	9.8	9.7		9.0
Maya blue	Indigo	14.2	12.8	400-850, 1840-2050	11.6
Guado (WOAD)		8.4	5.4		4.4

In multiple manuscript measurements, the areas of pigment on the mock manuscript were relatively small, meaning that the illumination spot and thus detection area would include not only the pigment but also portions of the surrounding blank paper. This could introduce additional reflectance signals unrelated to the pigment itself, potentially increasing the spectral angle mapping (SAM) score and leading to an overestimation of spectral differences. Those pigments that included paper in the area had a second spectra made by taking the papers log(1 / R) spectra away from that of the pigment. Also to mitigate this effect, a feature-based SAM approach was also employed: spectral regions associated with known absorption features of the pigments were isolated and compared separately. These spectral regions were selected by observation. By focusing only on these diagnostic features, the influence of spectral noise or unrelated contributions from the substrate (blank paper) was reduced, resulting in a more accurate assessment of pigment similarity.

A python script was the used to do SAM comparison of every pigment with every painted watercolour strip form a vintage colour chart, Washes of artists' water colours Winsor & Newton limited. Reflectance data was measured for the top and bottom of the 134 paint strips using the FORS probe. Measurements were taken at the top and bottom of each strip as there

was a slight gradient between the top and bottom of each strip the SAM value were calculated using the slightly more strongly absorbing top of the strips. The strips were organised in 6 plates, 5 of 24 and the sixth with the last 8. Table 5 shows some notable SAM values obtained.

Table 5: A table of the maximum and minimum SAM values for each plate and what pigment and water colour combination gave that value.

Plate	Maximum			Minimum		
	Max. SAM /° (1dp)	Pigment	Water colour	Min. SAM /° (1dp)	Pigment	Water colour
1	104.3	MgCO$_3$	Prussian green	7.1	Corn. Carmine red	Carmine lake
2	99.9	MgCO$_3$	Alizarin green	7.5	Corn. Red ochre	Indian red
3	103.5	MgCO$_3$	Prussian blue	5.9	Corn. Blue verditer	Antwerp blue
4	100.4	Zinc white	Blue black	2.6	Krem. Bone black	Charcoal gray
5	102.3	MgCO$_3$	Indigo	8.2	Corn. Yellow ochre	Roman ochre
6	104.0	MgCO$_3$	Chinese blue	9.2	Ald. Prussian blue	Chinese blue

Table 5 shows that MgCO$_3$ consistently produced the highest SAM scores across all plates, confirming previous observations. Overall, the maximum SAM scores for the watercolour samples are lower than those observed in the pure pigment comparisons, suggesting that the spectral differences between the watercolours are somewhat smaller. Similarly, the minimum SAM values are higher than in the pigment-only measurements, indicating a reduced dynamic range in spectral similarity. One possible explanation is that the watercolours contain additional compounds, such as binders, extenders, or other additives used to formulate paints, which could modify their spectral signatures compared to raw pigments.

Interactance spectroscopy

To investigate how localised absorbers influence spatially resolved reflectance, a series of interactance spectroscopy measurements were performed. Liquid phantoms with varying absorber distances beneath the surface were used to simulate different optical structures. Average reflectance was recorded as a function of SDS, enabling analysis of how absorption depth affects surface reflectance profiles.

## Experimental Interactance Spectra
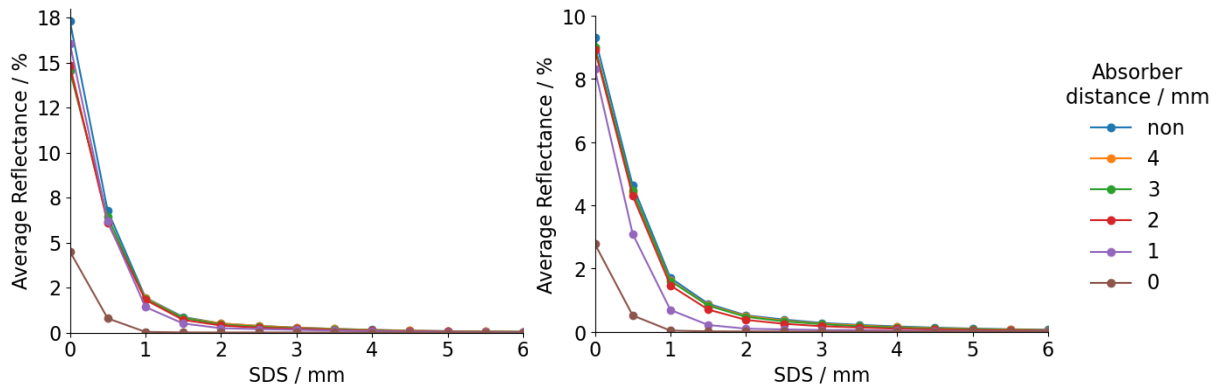
Figure 14: Average reflectance (%) versus source–detector separation (SDS) for liquid phantom experiments using milk-based samples. The left plot shows data collected from whole milk, while the right plot shows results for a 50:50 dilution of milk and water. In both cases, a black absorber (plastic piece) was placed at varying depths within the cuvette. The different curves correspond to different absorber distances beneath the surface, illustrating how absorber position affects the surface-reflected signal as a function of lateral separation.

For Figure 14 it is assume negligible absorption across all wavelengths as the average reflectance is over the entire visible range recorded. The data demonstrates that absorbers placed closer to the surface produce a more pronounced reduction in reflectance, particularly at small SDS values. However, the reflectance profiles show relatively discrete changes between different absorber depths. Ideally, the use of a greater number of intermediate absorber positions or more finely tuned absorber strengths would have allowed a more gradual transition in reflectance behaviour. This would enable a more detailed assessment of depth sensitivity and more accurate comparisons with diffusion-based models.
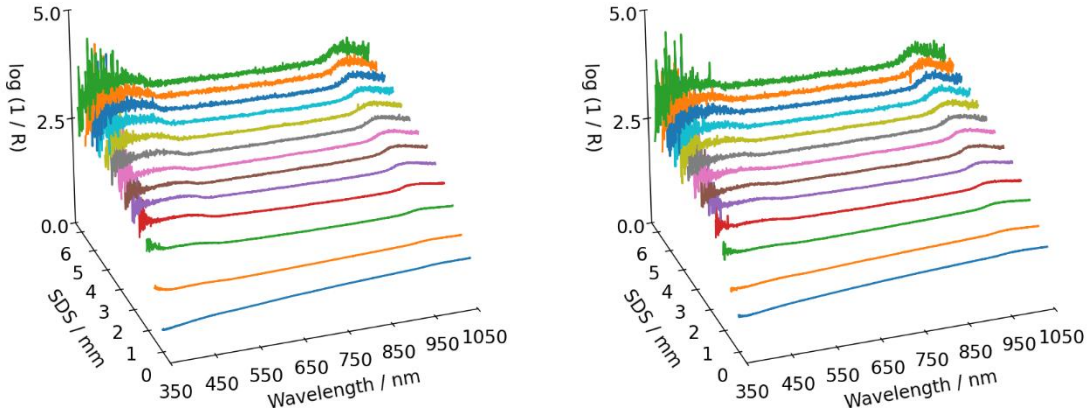
Figure 15: 3D plots of measured log (1/R) as a function of both SDS and wavelength for the liquid phantom (50:50 whole milk mixture). Left: sample = whole milk, Right: sample = 50:50, whole milk: water.

The log (1/R) value increases with both increasing SDS and increasing absorption (whole milk vs mixture), consistent with what is expected. Stronger absorption is observed at the longest and shortest wavelengths, with a more stable reflectance over a middle range of wavelengths.
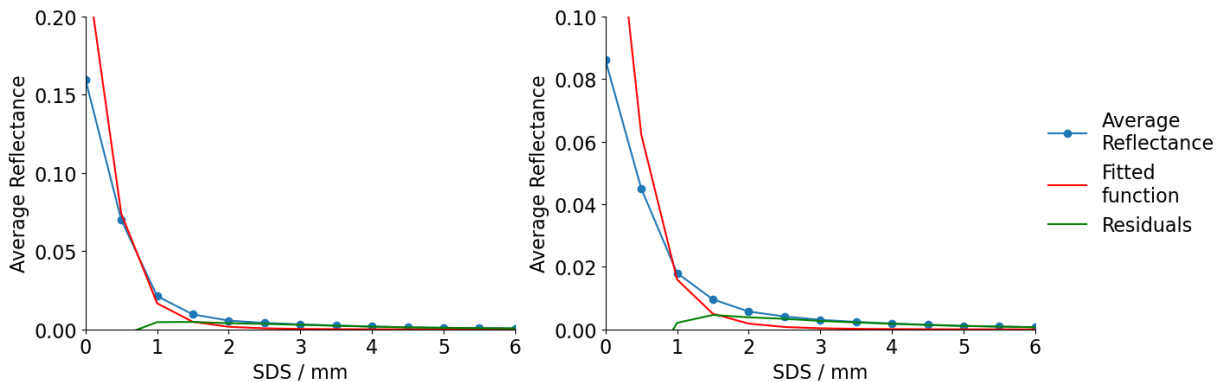
Figure 16: Measured relative reflectance as a function of source–detector separation (SDS) for the [sample type, e.g., 50:50 whole milk mixture]. The average reflectance decreases in an almost exponential decay with increasing SDS, consistent with photon diffusion behaviour. Left: sample = whole milk, Right: sample = 50:50, whole milk: water.

The interactance spectroscopy measurements of the 50:50 and milk samples show a decreasing trend in relative reflectance with increasing SDS (Figure 16). As expected from diffusion theory, photons that travel longer distances are increasingly attenuated due to scattering and absorption. The averaged reflectance is calculated over the range 600–800 nm, this is due to this range have the most stable reflectance values for comparison (Figure 15). This data has been fitted using equation 18 from Below table 6 shows the parameters obtained from the curve fitting.

Table 6: Tables of the optical parameters obtained from fitting the experimental data to Equation (18) of Farrell et al. (1992) [17].

Whole milk	Red scat	abs
	2.17277201	0.06707135
Standard error	16.77887679	1.45514265
Least squares	0.0060424681238396205	

50:50	Red scat	Abs
	1.94221656	0.0586159
Standard error	11.51680571	1.08873531
Least squares	0.007033798298787741	

These values physically make sense but the standard error of them is alarmingly large relative to the values. These least squares values show a good fit between the model and its parameters with the experimental data.

Simulated Interactance Spectra
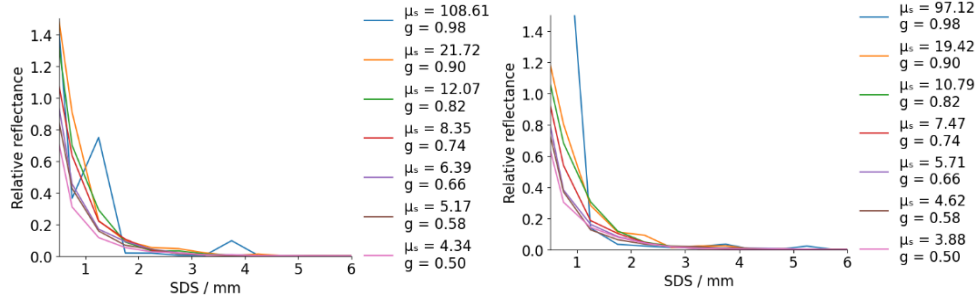
Figure 17: Plots of simulated relative reflectance vs SDS for a parameter sweep of values that satisfy the reduced scattering coefficient obtained from the experimental curve fitting. Left: sample = whole milk, Right: sample = 50:50, whole milk: water.

These graphs (Figure 17) of ranges of scattering coefficients and anisotropy show very small spread with anomalous curves for very high scattering and anisotropy factors. These sporadic lines are likely due to very few photons contributing to the relative reflectance at medium SDSs thus the sampling is not an accurate representation of what might happen. This low lateral spread is again due to the very short step lengths and very small deviation in direction. The tight spread of the other curves makes sense and supports the ideas discussed in Farrell et al. (1992) about how photon migration being described by the reduced scattering and absorption coefficients. This result shows that for a fixed reduced scattering coefficient there is little deviation in results from small changes in the optical parameters that make it up. These results might be explainable as the increasing anisotropy increase lateral spread thus slightly higher relative reflectance values at further SDSs but only a slight increase as the increased scattering coefficient works in the opposite way to decrease the spread. Anisotropy is shown to be slightly more important in the simulation as there is a small trend of increasing reflectance at higher g values.

## Comparison Between Experiment and Simulation
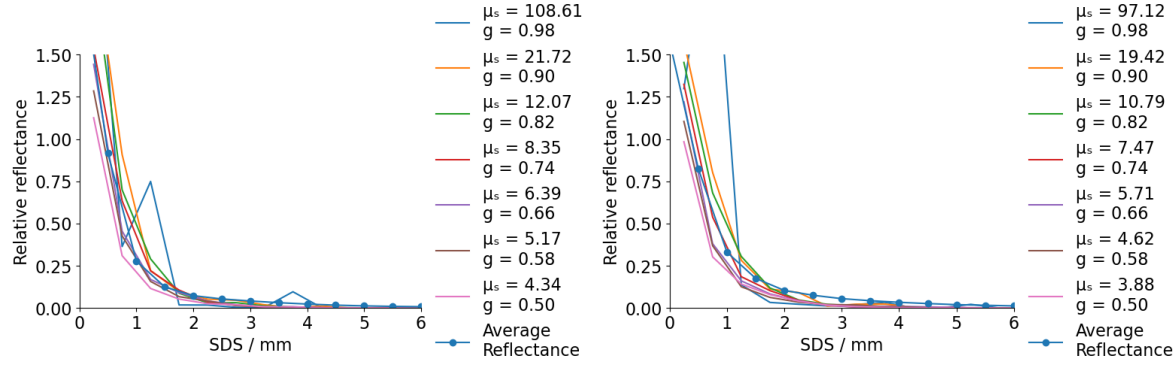
Figure 18: Plots of simulated relative reflectance vs SDS for a parameter sweep of values that satisfy the reduced scattering coefficient with the experimental relative reflectance curve superimposed and normalised to a similar magnitude to them. Left: sample = whole milk, Right: sample = 50:50, whole milk: water.

The comparison between the experimental interactance spectroscopy data and the Monte Carlo simulations with varied scattering coefficients (μ_s) and anisotropy factors (g) reveals that simulations with moderately high scattering and anisotropy values provide the closest agreement with the measured reflectance profiles. While simulations with the very highest μ_s and g values begin to diverge slightly, likely due to excessive forward scattering and reduced lateral photon migration, those with slightly elevated values above the baseline ($g = 0.9$, $\mu_s = 19.42$ for the 50:50 mixture) match the experimental trend more closely across the range of source–detector separations (SDS). This suggests that the optical properties of the sample are best represented by moderately high reduced scattering and anisotropy parameters, consistent with the behaviour expected for turbid, scattering-dominated media such as diluted milk. These findings reinforce the validity of the curve-fitting approach and the general consistency between experiment and simulation. Also, there is little difference between the two samples both beginning closer to the higher scattering coefficients, one would expect a greater scattering coefficient for the whole milk sample due to a higher density of scatterers.

The plots in Figure 19 illustrate the weighted average depth of photon penetration as a function of radial distance for different optical parameter sets, corresponding to fitted scattering anisotropy values of 0.92, 0.96, 0.94, and 0.9 in subplots (a), (b), (c), and (d), respectively. These results were obtained by running Monte Carlo simulations using fitted optical parameters derived from the milk-based liquid phantom samples. Generally, higher anisotropy (g) values (e.g., 0.96) lead to more forward-peaked scattering, resulting in shallower average penetration depths at a given radial distance, as observed in plot (b) compared to lower anisotropy cases like (d). Comparing these trends to the experimental

average reflectance plot, where the effect of placing absorbers at different depths was measured, we observe good qualitative agreement: absorbers positioned closer to the surface resulted in larger reductions in reflectance at small source-detector separations (SDS), mirroring the shallower penetration depths predicted for more forward-scattering media. Both the depth analysis and the reflectance measurements indicate that the photon sampling volume becomes increasingly shallow with higher scattering anisotropy or with the presence of near-surface absorbers. This consistency validates the use of the fitted optical parameters for modelling depth sensitivity and supports the link between photon migration depth and SDS observed experimentally.
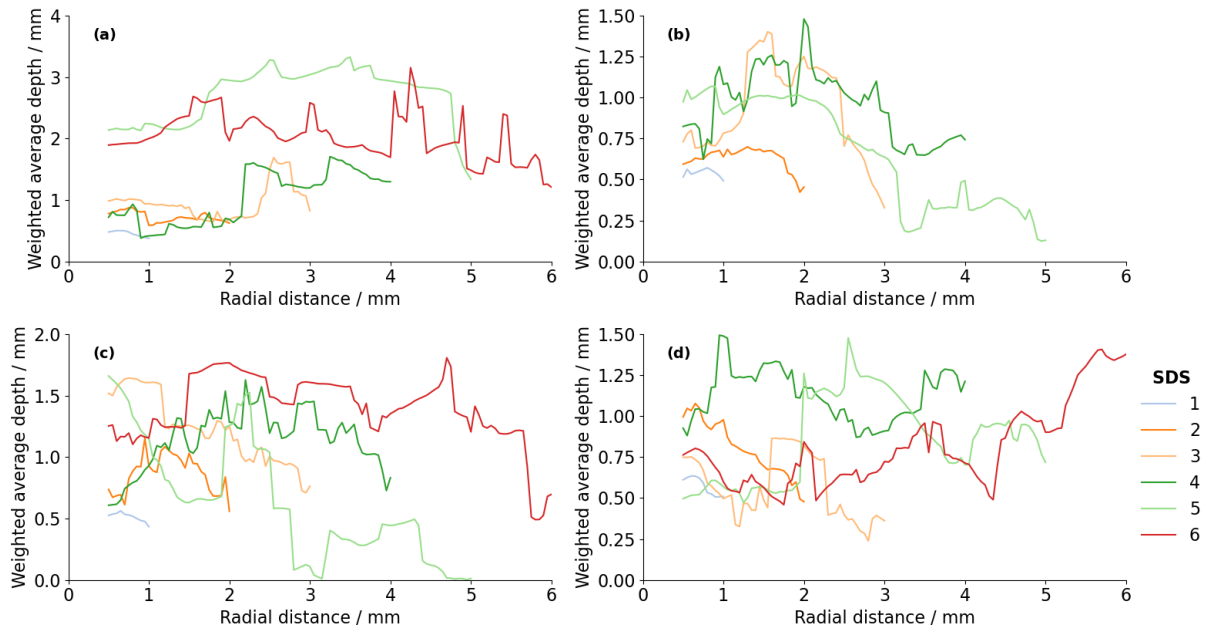
Figure 19: Weighted average photon penetration depth versus radial distance for Monte Carlo simulations based on fitted optical parameters derived from liquid phantom experiments. (a) g = 0.92, (b) g = 0.96, (c) g = 0.94, (d) g = 0.90. Each curve represents a different detector offset (SDS). Increasing radial distance generally leads to increased average photon depth, with higher anisotropy values causing shallower penetration overall. These trends agree with experimental reflectance data, where closer absorbers reduced detected reflectance at small SDS, confirming the dependence of depth sensitivity on both optical properties and measurement geometry.

Conclusions and suggestions for future work

This project demonstrated how spatially resolved reflectance measurements and Monte Carlo simulations can be used together to investigate photon migration in turbid media. The fitted optical parameters showed good consistency between experiment and simulation, validating the methodology and confirming trends expected from diffusion theory. Future work could involve improving the experimental setup by refining source geometry and incorporating time-resolved

measurements, allowing even deeper insights into photon path distributions. Additionally, expanding the phantom models to include layered structures or heterogeneous inclusions would better simulate real-world materials like biological tissue or historic paintings.

Experimental

Reflectance spectroscopy

Initially the effect of concentration of absorbers on reflectance was investigated. These samples were made by painting a layer of link on a paper substrate. These samples provided a qualitative range of absorber concentrations, as the manual painting process does not ensure consistent ink deposition. Consequently, samples with a higher number of layers do not necessarily exhibit greater absorbance; for instance, six heavily applied layers may contain more absorber than seven lightly applied ones. To mitigate this problem samples were made by adding subsequent layers to small areas of previous samples so that with increasing number of layers the concentration of absorber increases (qualitatively). Visible reflectance data of samples were recorded from 350 – 1050 cm^{-1} using: 1. a halogen light source, HL-2000-FHSA-HP from Mikropack, 2. a blue lens filter (to partially absorb longer wavelength light and flatten spectra), 3. fibre optic cables, a three dimensional translation stage (to focus the detector fibre / lens), 4. fibre optic lenses, 5. a high sensitivity spectrometer, Maya 2000 PRO from Ocean Optics (Figure 19). The incident beam is at approximately 45-degrees from perpendicular to the surface (the detector) so that no specular reflection is captured only diffuse reflectance. For all spectroscopic measurements a white Spectralon® (99% reflectivity) tile was used to either provide a reference spectrum of the light source or to set the reference in the program, to allow the reflectance spectrum to be measured by dividing the sample spectra by that of the reference.
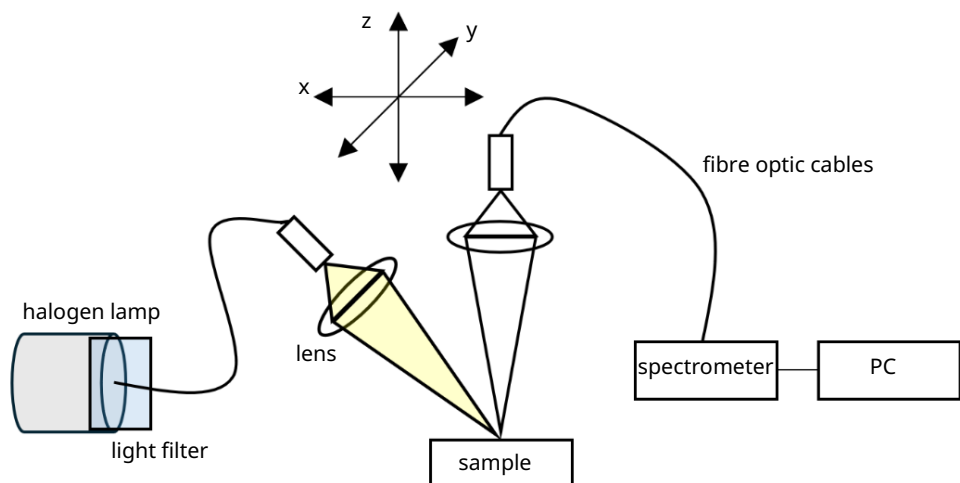

Figure 29: A diagram of the experimental setup used to measure visible reflectance spectra.

For each spectra a measurement was taken with the lamp turned on and off and this allowed for any background light to be removed from the data. A reference white spectrum was used to normalise the results:

$$Reflectance_{sample} = \frac{Sample_{light} - Sample_{dark}}{Reference_{light} - Reference_{dark}} \qquad (1)$$

A similar instrument was used to collect the reflectance spectra over a greater range of wavelengths using a fibre optic reflectance spectra (FORS) probe, this allowed for the investigation over a greater range by using a mirror to reflect some of the reflected light from the sample into a Fourier transform infrared (FTIR) spectrometer. A Maya 2000 PRO spectrometer is used to record visible light spectra from $400 - 1050$ cm^{-1} and the FTIR spectrometer from $800 - 2500$ cm^{-1}. The software then combined and displayed both spectral line shapes as one spectrum. Another change from figure 1 is that two oppositely facing beams of incident light from the same light source at approximately 35-degrees to the normally incident detector fibre. (Figure 20)
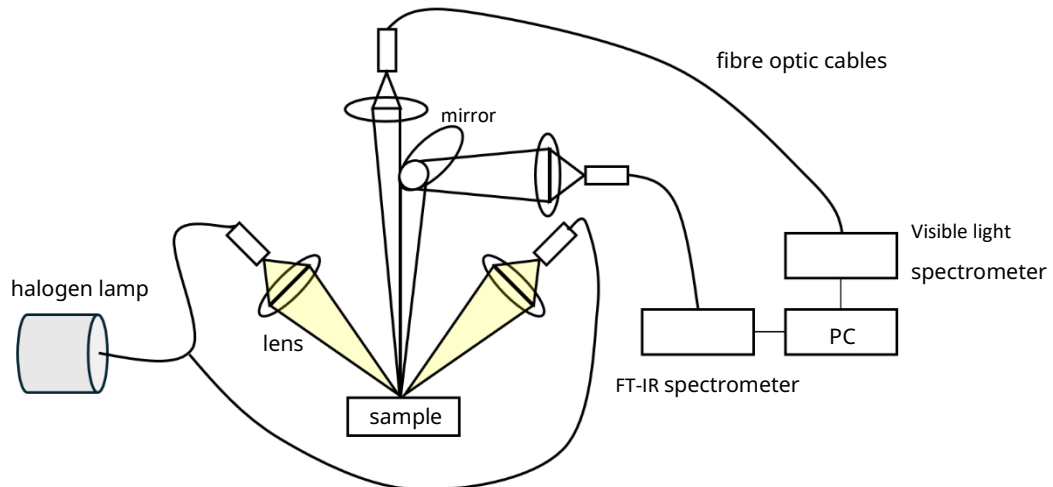
Figure 30: A diagram of the FORS probe used to measure visible – IR reflectance spectra.

We were interested in making a spectral library of known pigments which can be used to determine what pigments were used in antique painting and manuscripts by comparison with the known pigments' spectra. To create the samples of known pigments it was decided to make them a mixture of a non-absorbing (in the wavelength range of interest) compound, NaCl, with the pure pigment in a two to one weight ratio this ensured that the samples were not too strongly absorbing as that could lead to a loss in sensitivity and an increase in noise. Each component was ground down into a fine powder using a pestle and mortar to ensure that they were fully mixed. All samples were made sufficiently deep so that they were effectively infinite. This was due to the highly scattering properties of the blank compound NaCl and the pigments themselves. The data acquired from these experiments were transformed using log(1 / R) as a

substitute for absorbance, this approach has been proven to be empirically effective in sample concentration correlation work by Norris (2005)[24] for composition analysis of turbid media. This approach was thought to be applicable to most of the experiments here as the samples used were ensured to be optically thick thus transmittance was negligible and the proportion of light that was reflected back in the detection spot is very high.

Interactance spectroscopy

Experiment

To perform spatially resolved reflectance measurements (interactance spectroscopy), an experimental setup similar to figure 20 was employed, with key modifications to enable source-detector separation (SDS) control, to rotate the whole setup vertically for liquid samples and removing the second spectrometer. The detector fibre was attached to a precision 3D translation stage and was incrementally repositioned along the x-axis relative to a fixed illumination point. Measurements were taken in 0.5 mm steps from 0 to 6 mm lateral separation, yielding a reflectance vs SDS profile. This configuration approximates the geometry assumed in diffusion-based models, where spatially offset detection provides depth-sensitive reflectance data. The main difference between the setup used and diffusion models was the use of two source beam at ~28 degrees to the normal to the surface, diffusion models such as those referred to here typically use a single pencil beam normal to the surface. This difference in sources is likely to cause different results and inaccuracies at short SDSs as multiple scattering events are not likely to have occurred. The difference is also likely to affect results more or less depending on the parameters used, for example large anisotropy values increases the dependence on the initial direction of the photons. There would be more difference in the results if absolute values were calculated and modelled by this project and by the relevant papers. but since the project and the papers of relevance. For liquid phantoms a cuvette containing either whole milk or a 50/50 milk-water dilution was used. The cuvette (internal dimensions ~$10 \times 10 \times 40$ mm) was assumed have little optically affect due to its high transparency and negligible extinction across the measured spectral range (350 – 1050 nm). The data being collected was relative reflectance data so if the cuvette was weakly absorbing or scattering this would reduce all recorded measurements equally not affecting their relative positions but would decrease the signal to noise ratio. Additionally, its walls were thin enough to avoid introducing significant refraction or boundary effects. A Maya 2000 PRO spectrometer (Ocean Optics) was used to record these spectra along with a

Spectralon® 99% reflectance tile serving as the white reference. For every sample spectrum four measurements were needed to use Equation (1) again, a light and dark spectra of the white reference tile and for the sample.

Equation (18) of Farrell et al. (1992) [17] was fitted to the interactance spectra to determine the absorption and reduced scattering coefficients (μ_a and μ'_s respectively) for later use in a Monte Carlo (MC) simulation. Since the code uses the scattering coefficient and anisotropy factor separately and not in the reduced scattering coefficient's combined form and a variety of different combinations of the values were simulated. To allow for an accurate fit to the model equation the reflectance spectra at 0mm SDS was excluded as it violates the diffusion theory used by the model and the measurement at 0.5mm was also excluded as put this in results and discussion.

Monte Carlo simulation

An MC simulation approach was also used to study photon paths during diffusion in turbid media. The simulation aimed to produce similar and comparable results to that of the experiments while also providing a wider look at a range of different optical parameters in terms of their effect on relative surface reflectance and photon path depth as well as investigating photon paths as the SDS changing, keeping the optical parameters constant.

Simulation Framework

The simulation aimed to further the model presented by Groenhuis *et al.* (1983).[3] Their paper provided relative reflectance data from the statistical sampling of each individual scattering event, this part of the project sought to provide similar data and also track and analyse the paths of the photons. The code simulates one photon at a time from its generation at the source with its initial direction and distribution determined by the source, through multiple scattering events with absorption taking place between those points. For the statistical sampling and to account for absorption each photon is give an initial weight of one which is reduced by absorption during each step. Weight is also used to increase efficiency and reduce computational time and resources. The simulation terminates the photon being simulated if its weight falls below a critical weight this should have negligible effect as photons with a lower weight contribute less to the sampling and probability calculations used. Another termination check is implemented which compares the photons position to a three-dimensional boundary so that if the photon has travelled a large distance away from the area of interest it is terminated. This has negligible

35

effect on the error as the contribution made in sampling considers the photons depth. Both provide minor statistical error, but this is diminished by them allowing for more photons to be simulated. Figure 21 provides a flowchart describing the structure and steps of the code.
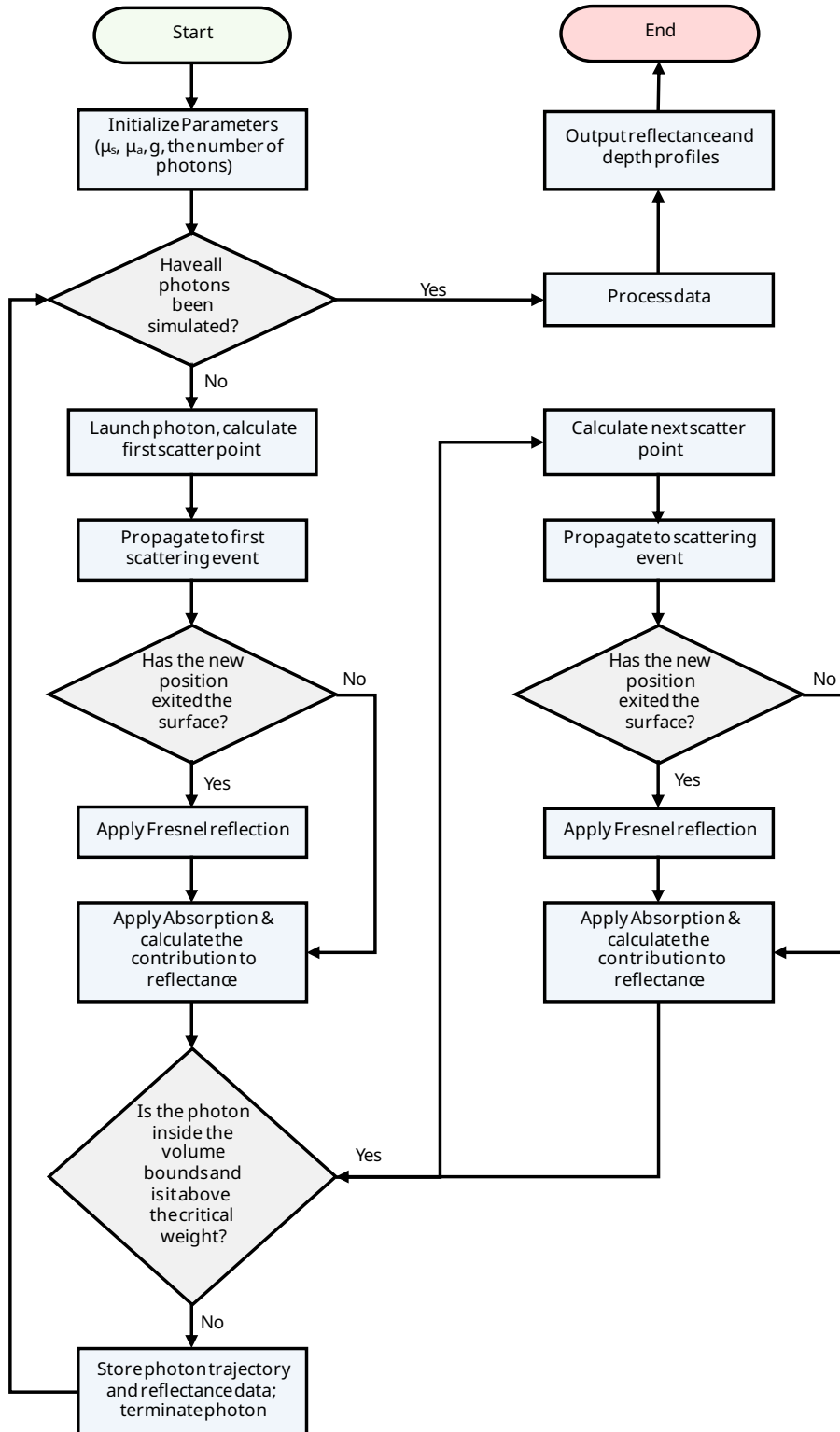
Figure 21: A flowchart describing the Monte Carlo photon migration simulation used to model interactance spectroscopy.

Simulation summary:

(For this summary and for the parameter sweeps in the Results and Discussion section the source geometry is a collimated beam that is 1mm in diameter and perpendicular to the surface)

1. **Initialize Parameters**

   Optical properties (μ_a, μ_s and g) are defined as well as the source geometry. Critical weight and boundaries for photon termination are set.

2. **Generate a Photon**

   Each photon starts at a random location within the source spot. The initial direction is vertically into the surface with random azimuth. The photon weight is set to one.

3. **Sample Step Size**

   A random step length d is sampled from an exponential distribution:

   $$d = \frac{-ln\,(RN)}{\mu_s}$$

where RN is a random number uniformly distributed between 0 and 1. This models the random distance to the next scattering event.
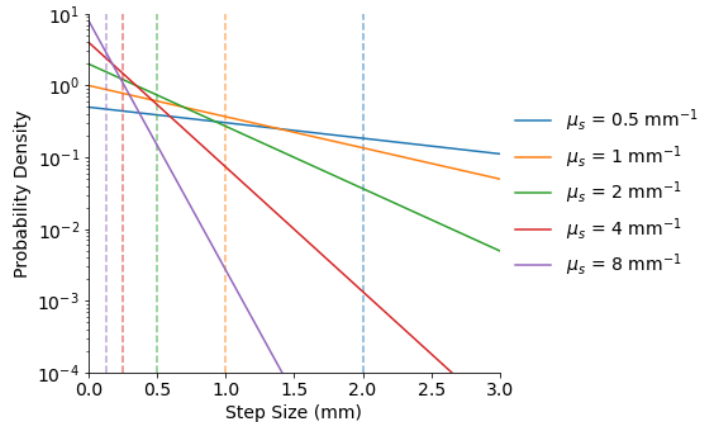
Figure 22: A plot showing the distribution of step size for different scattering coefficients. The dashed lines shown the mean free path lengths.

4. **Propagate Photon**

   Using the step length d and direction (defined by the directional/scattering and the azimuthal angles), the photon's Cartesian coordinates are updated.

5. **Surface Interaction Check (Fresnel Reflection)**

   If the photon crosses the surface (z < 0), it is reflected back into the medium with a new weight determined by the Fresnel reflection coefficient. The probability of reflection depends on the angle of incidence and refractive index mismatch (milk-water ~1.35 vs air ~1.0).

6. **Absorption**

   The photon's weight is reduced to account for absorption along its path between scatter points:

   $$W_{new} = W_{old} \cdot e^{-\mu_a \cdot d}$$

7. **Calculate Reflectance Contribution**

   At each scatter point, the probability that the photon would scatter towards the surface and be detected is calculated using the Henyey-Greenstein phase function[8]:

   $$P(cos\theta) = \frac{1 - g^2}{(1 + g^2 - 2g\, cos\theta)^{3/2}}$$
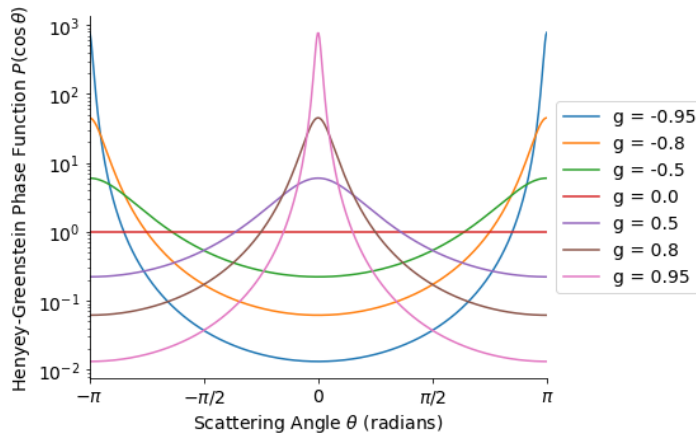
Figure 23: A plot showing the relationship between the Henyey-Greenstein phase function and scattering angle for varying anisotropies.

Increasing g shifts scattering toward the forward direction, making the distribution more forward peaked meaning that the photon is more likely to continue travelling in a similar direction. This effects the contribution to reflectance as this function is being used to see how probable the upward detection direction is based on the current direction and g. The phase function is multiplied by the projected solid angle from the point to an area on the surface, the photon's weight and function describing the probability of the photon travelling that path without being scattered or absorbed.

8. **Termination Checks**

   If the photon's weight drops below the critical threshold, or if the photon moves beyond the maximum allowed spatial boundaries, it is terminated. And step 2 is repeated generating the next photon.

9. **Sample New Scattering Angle (Henyey-Greenstein Sampling)**

   The scattering angle θ is randomly sampled based on the anisotropy factor g using inverse transform sampling and the azimuthal angle φ is generated as a random number between 0 and 2π:

$$cos\theta = \frac{1}{2g}\left(1 + g^2 - \left(\frac{1-g^2}{1-g+2g\,RN}\right)^2\right)$$

$$\varphi = RN \cdot 2\pi$$

where RN is a new random number uniformly distributed between 0 and 1 which is reselected before each use.

New direction cosines are calculated from θ and azimuth φ.

10. **Store Data**

    Each photon's scattering events, depth history, and its contributions to reflectance are recorded for post-processing.

11. **Multiple Scattering**

    Steps 3 to 10 are repeated until the photon is terminated.

12. **Data Processing for Output**

    After all photons have been run:

    -Reflectance contributions are sorted by radial source-detector separation (SDS) bins. This method is chosen since this source geometry is cylindrically symmetrical.

    -For more detailed path analysis, photon trajectories are interpolated along the radial direction to calculate mean depth as a function of radial distance.

Each simulation simulated $\geq$ 10,000 photons to ensure statistical robustness. The simulations with a low scattering coefficient, a high absorption coefficient or a high anisotropy factor were ran with 50,000 photons as those conditions lead to fewer scattering points thus less computational memory and time were needed allowing for a higher number of photons.

Parameter Sweep and Model Characterization

Simulations were conducted across a broad range of optical properties to evaluate general behaviour and verify physical consistency with published results (e.g. Groenhuis et al., 1983), before applying fitted experimental parameters. These parameter ranges were used:

- Anisotropy factor (g): -0.9 to 0.9
- Absorption coefficient (μ_a): 0.01 to 1.5 mm^{-1}
- Scattering coefficient (μ_s): 0.5 to 20 mm^{-1}

For each set of optical parameters, the following plots were created:

• Relative reflectance vs Source Detector Separation (SDS): Reflectance profiles were generated by summing the contribution of each scattering point in each SDS radial bin, allowing

comparison between different scattering coefficients, absorption coefficients, and anisotropy values.

• Weighted average penetration depth vs radial distance: For each SDS bin, the weighted average depth of photon paths at different radial distances was calculated and plotted, providing insight into how the depth of photon penetration changes as the SDS changes. The weight is determined by the reflectance contribution of that path to that radial bin and is normalised with the path with the highest probability fully contributing to the weight average.

• Parameter-sensitivity plots at fixed detector location: For selected SDS values, the average path of different optical parameter sets (varying μ_s, μ_a, or g individually) were generated to investigate how each optical property influences penetration.

While full depth histograms for every interpolated slice were not computed due to processing constraints, the combination of averaged depth and spread provides a robust summary of depth sensitivity across conditions.
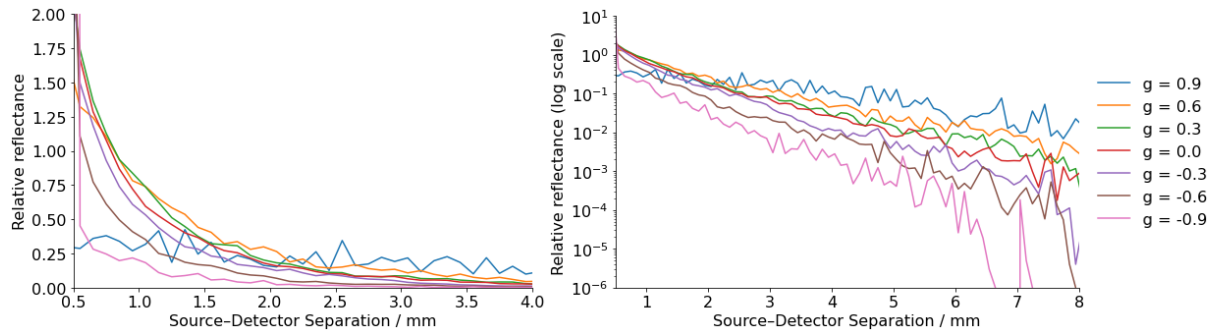
Figure 23: Relative reflectance vs SDS plots for varying anisotropy factors, with fixed absorption and scattering coefficients (0.01 mm⁻¹ and 10 mm⁻¹ respectively). Left plot: linear scale, Right plot: uses logarithmic scale to highlight attenuation at larger separations.

Higher anisotropy values (e.g. 0.9 and 0.6) result in greater reflectance at larger separations due to broader photon migration because the likelihood of each scattering angle to be forward is greater, for example 0.9 not having the typical exponential decay seen in the other plots. Lower g values lead to faster attenuation due to more backward scattering, reducing the likelihood of photons reaching distant detectors as they keep backtracking over the same radial distances.
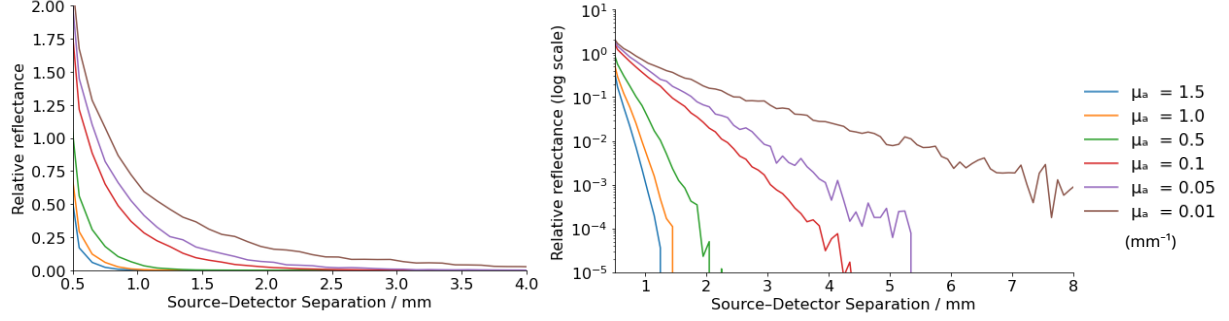
Figure 24: Relative reflectance vs SDS plots for varying absorption coefficients, with a fixed scattering coefficient and anisotropy factor (10 mm⁻¹ and 0 respectively). Left plot: linear scale, Right plot: uses logarithmic scale.

Figure 24's plots illustrate how increasing absorption affects the spatial distribution of reflectance in a turbid medium. As μ_a increases, photons are more likely to be absorbed before reaching the detector, resulting in a steeper decay of reflectance with SDS. The log-scaled version (right) highlights how higher-absorption media (≥ 0.5 mm⁻¹) very quickly suppress photon migration beyond 2–3 mm. At low μ_a values, reflectance decays more gradually, allowing deeper photon penetration.
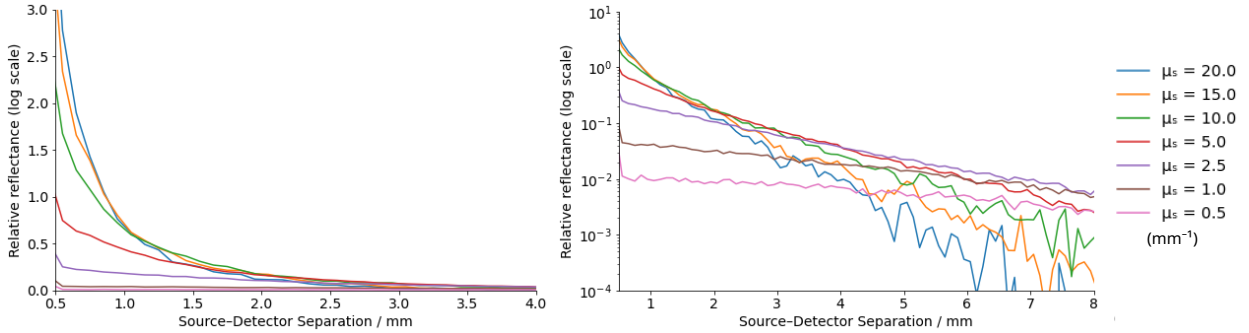
Figure 25: Relative reflectance vs SDS plots for varying scattering coefficients, with a fixed absorption coefficient and anisotropy factor (0.01 mm⁻¹ and 0 respectively). Left plot: linear scale, Right plot: uses logarithmic scale.

Figure 25 demonstrates how changes in the scattering coefficient (μ_s) influence reflectance across SDS. At high μ_s values (≥ 15 mm⁻¹), photons undergo frequent scattering and are more likely to be redirected back toward the detector at shorter separations, resulting in steeper attenuation and lower reflectance at larger SDS. Conversely, lower scattering (e.g. 0.5–2.5 mm⁻¹) permits longer photon paths, producing broader distributions and higher relative reflectance beyond 3 mm SDS.

Overall, these plots show that each parameter effects the relative reflectance at varying SDSs, with the shape more determined by μ_s and g and the amplitude is more determined by μ_a.
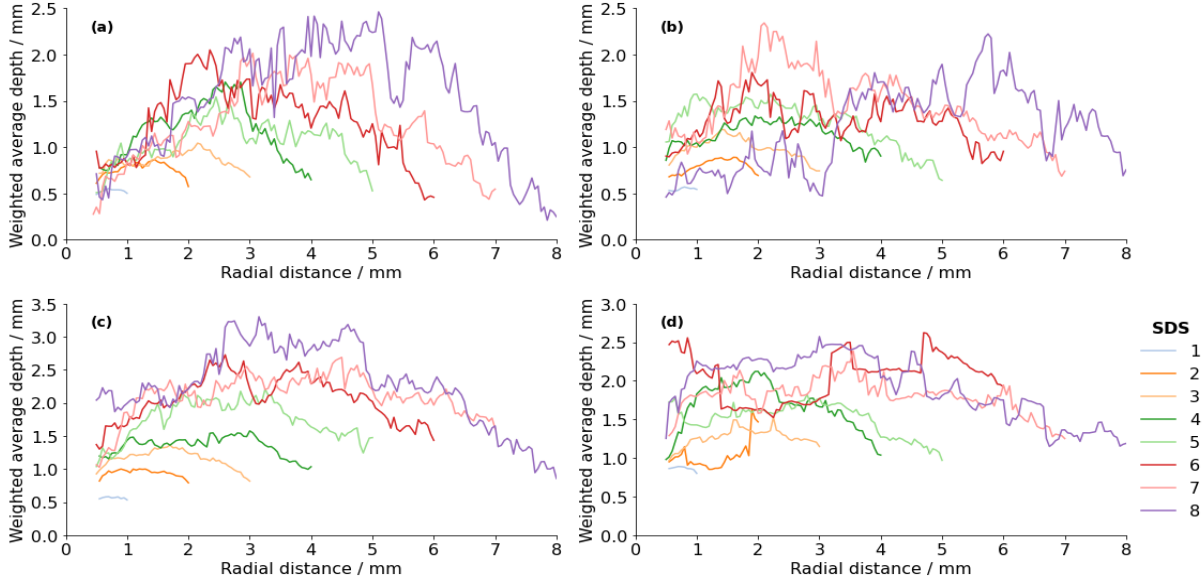
Figure 26: Plots showing how mean photon paths change for a range of anisotropy values at fixed absorption (μ_a = 0.01 mm⁻¹) and scattering (μ_s = 10 mm⁻¹). Each subplot shows the weighted average photon penetration depth as a function of radial distance for a given SDS. (a) g = -0.6, (b) g = 0.0 (isotropic scattering), (c) g = 0.6, and (d) g = 0.9.

These plots perform as expected in terms of the rough trend of increasing SDS leading to greater photon penetration (Figure 26). This trend is more closely followed for moderate absolute *g* values but compares less accurate for highly forward peaked or isotropic scattering. Comparing the plots of the absolute *g* value of 0.6 it is interesting that as expected the positive moderate *g* value had greater penetration (~40% more) than the -0.6 value yet they still follow the same trend seen for SDS and penetration depth.
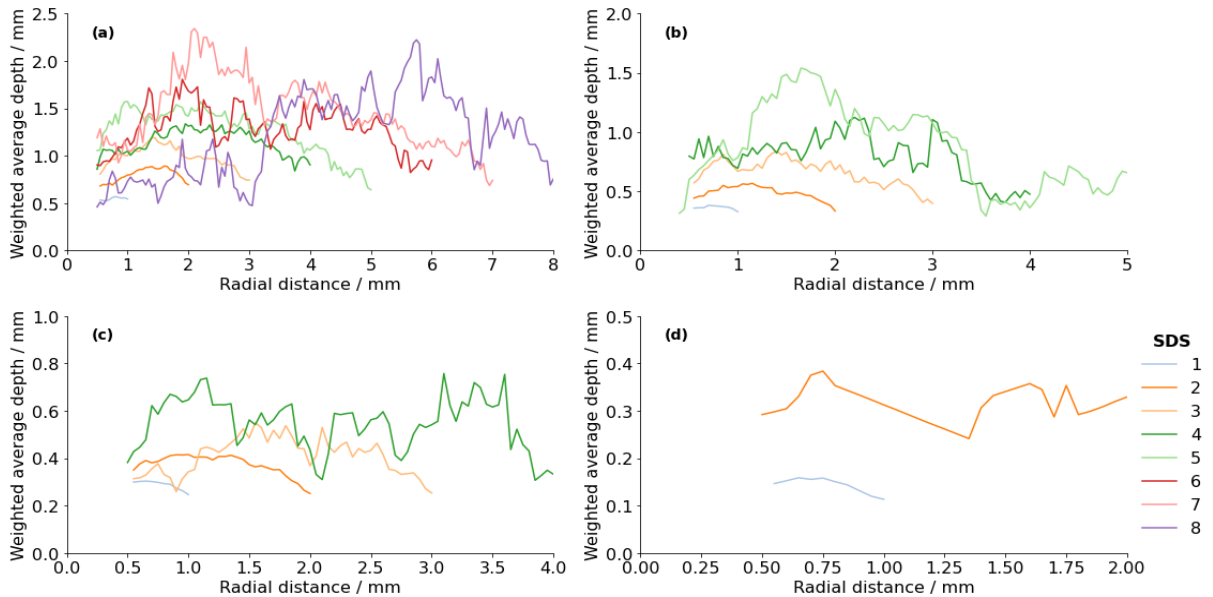
Figure 27: Plots of simulated depth sensitivity profiles for a range of absorption coefficients (μ_a) at fixed anisotropy (g = 0.0) and scattering (μ_s = 10 mm⁻¹). Each subplot shows the weighted average photon penetration depth as a function of radial distance for a given SDS. (a) μ_a = 0.01 mm⁻¹, (b) μ_a = 0.05 mm⁻¹, (c) μ_a = 0.1 mm⁻¹ and (d) μ_a = 1.0 mm⁻¹

43

These plots follow the trend seen in the previous plots of relative reflectance against SDS for variable absorption coefficients (Figure 24), in that for large μ_a values little to no signal is seen as SDS increases beyond 4mm. Increasing absorption coefficient is also shown to decrease penetration depth of all paths. These trends combine so that for the most absorbing simulated sample the SDSs that do have signal have reduced penetration and the most penetration paths (larger SDSs) have no or very little reflectance. These outcomes are as expected as they show a strong attenuation which is due to the exponential absorption used in the simulation. This highlights the challenge of probing deeper layers in strongly absorbing media using spatially-resolved reflectance spectroscopy.
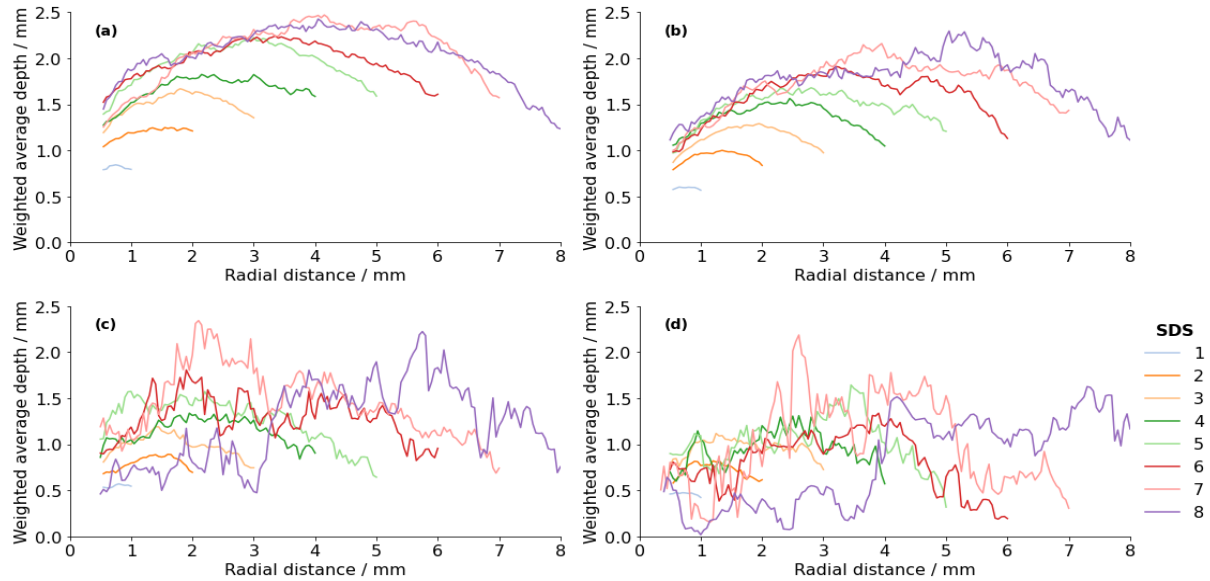
Figure 28: Plots showing how path depth changes for a range of scattering coefficients at fixed absorption (μ_a = 0.01 mm^{-1}) and anisotropy (g = 0.0). Each subplot shows the weighted average photon penetration depth as a function of radial distance for a given SDS. (a) μ_s = 1 mm^{-1}, (b) μ_s = 5 mm^{-1}, (c) μ_s = 10 mm^{-1} and (d) μ_s = 20 mm^{-1}.

For higher scattering coefficients (μ_s) the reflectance is more localised around the source as the distance between each scattering point is much smaller ($step\ length = -ln\,(RN)/\mu_s$). A scattering coefficient of 20 mm^{-1} also had the opposite effect as previous simulations in that the path for 8mm SDS had much lower penetration This may be due to a very low sample size at that large SDS as the probability of photons migrating that far with the very short step lengths is very small, this explanation is supported by the sporadic noise of the lines in this plot. This is supported by the very low relative reflectance seen in Figure 25.
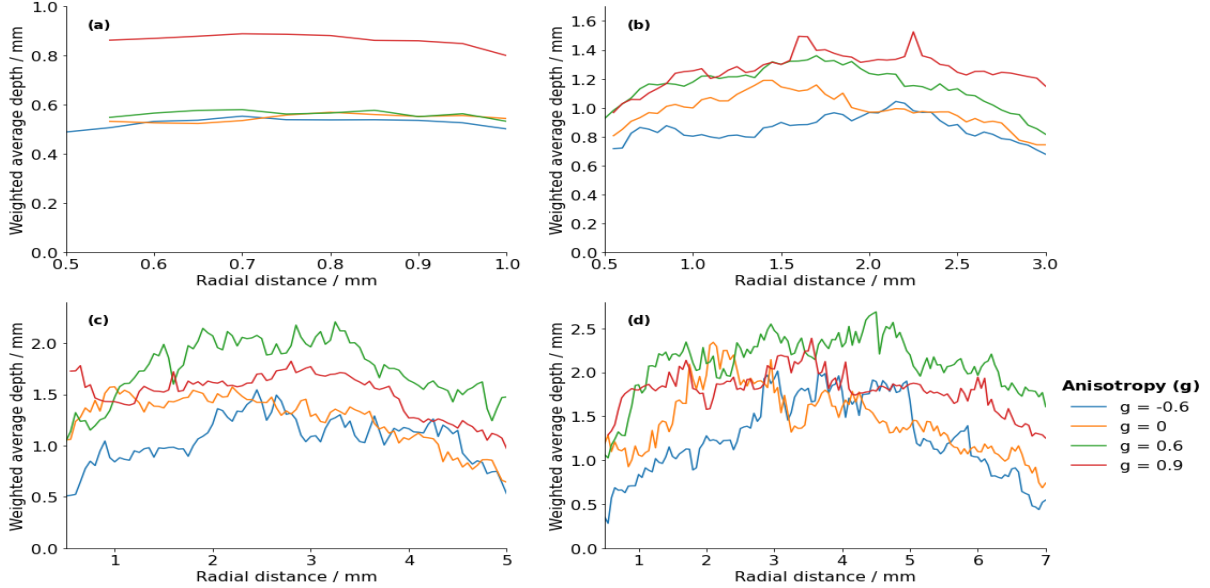
Figure 29: Plots of simulated photon paths for varying anisotropy factors (g) with fixed absorption (μ_a = 0.01 mm^{-1}) and scattering (μ_s = 10 mm^{-1}) coefficients. Each subplot shows the weighted average photon depth as a function of radial distance for a different SDS. (a) SDS = 1 mm, (b) SDS = 3 mm, (c) SDS = 5 mm, and (d) SDS = 7 mm.

Again, we see increasing anisotropy promote deeper photon migration and broader lateral spread due to more forward-directed scattering. At small SDS values (e.g., 1 mm), depth sensitivity remains relatively shallow and shows limited variation with g, as photons have fewer scatter points which means fewer opportunities to change angle. As SDS increases (e.g., 5–7 mm), differences become more pronounced: photons in highly forward-scattering media penetrate substantially deeper than those in more isotropic or backward-scattering conditions. This behaviour reflects the longer step lengths and reduced scattering angles associated with high anisotropy. Overall, these results reemphasize that anisotropy plays an important role in governing both the depth and breadth of photon sampling, particularly at larger source–detector separations where multiple scattering events accumulate.

Figure 30 again highlights that increasing absorption coefficient (μ_a) progressively suppresses photon migration depth and lateral spread due to its exponential nature. At small SDS (e.g., 1 mm), average photon penetration is shallow and shows limited variation with μ_a, as short travel distances reduce the cumulative impact of absorption. However, at larger SDS values, strong absorption (e.g., μ_a = 1 mm^{-1}) substantially restricts path depth compared to lower-absorption conditions (μ_a = 0.01 mm^{-1}). This behaviour reflects the exponential attenuation of photon fluence with pathlength, disproportionately affecting longer trajectories. Thus the reduced reflectance but also reduced penetration of detectable photons the photons that travel

deeper into the sample have travelled a further distance and so are more likely to be absorbed.
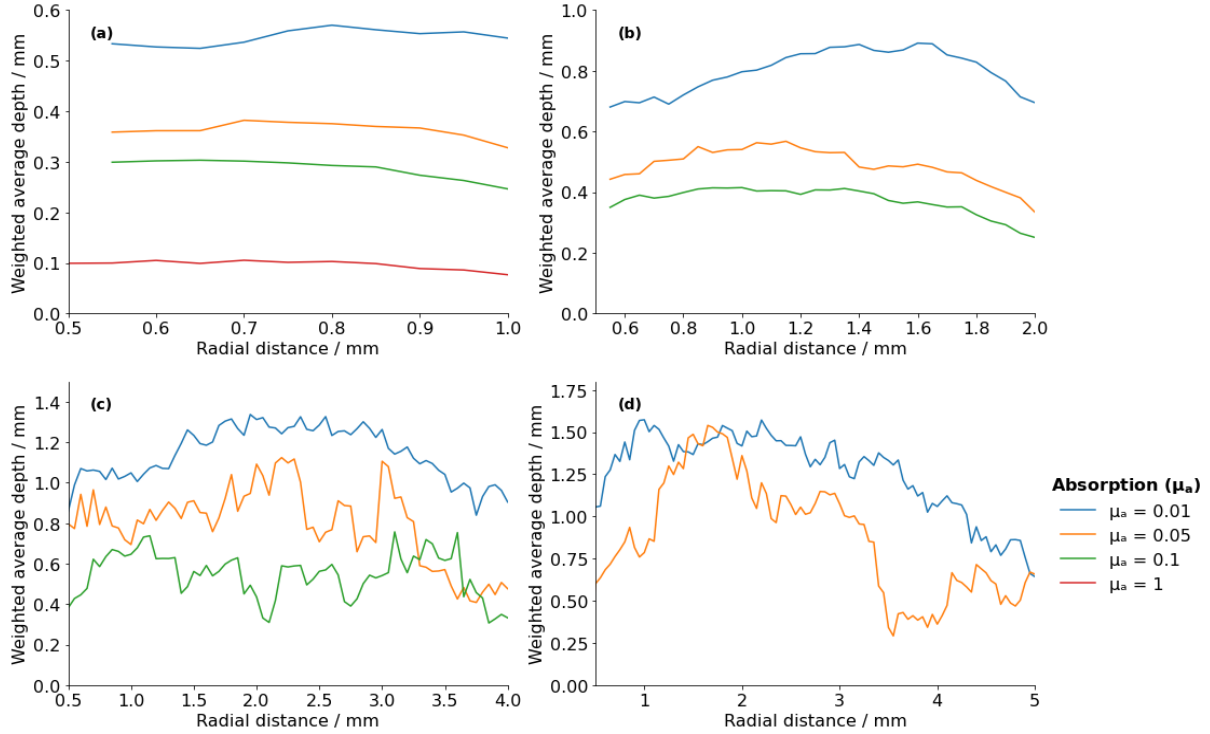
Figure 30: Simulated depth sensitivity profiles at fixed scattering ($\mu_s = 10$ mm^{-1}) and anisotropy ($g = 0$) for varying absorption coefficients (μ_a). Each subplot shows the weighted average photon penetration depth versus radial distance from the source for different μ_a values. The subplots correspond to the SDSs: (a) 1 mm, (b) 2 mm, (c) 3 mm, and (d) 4 mm.
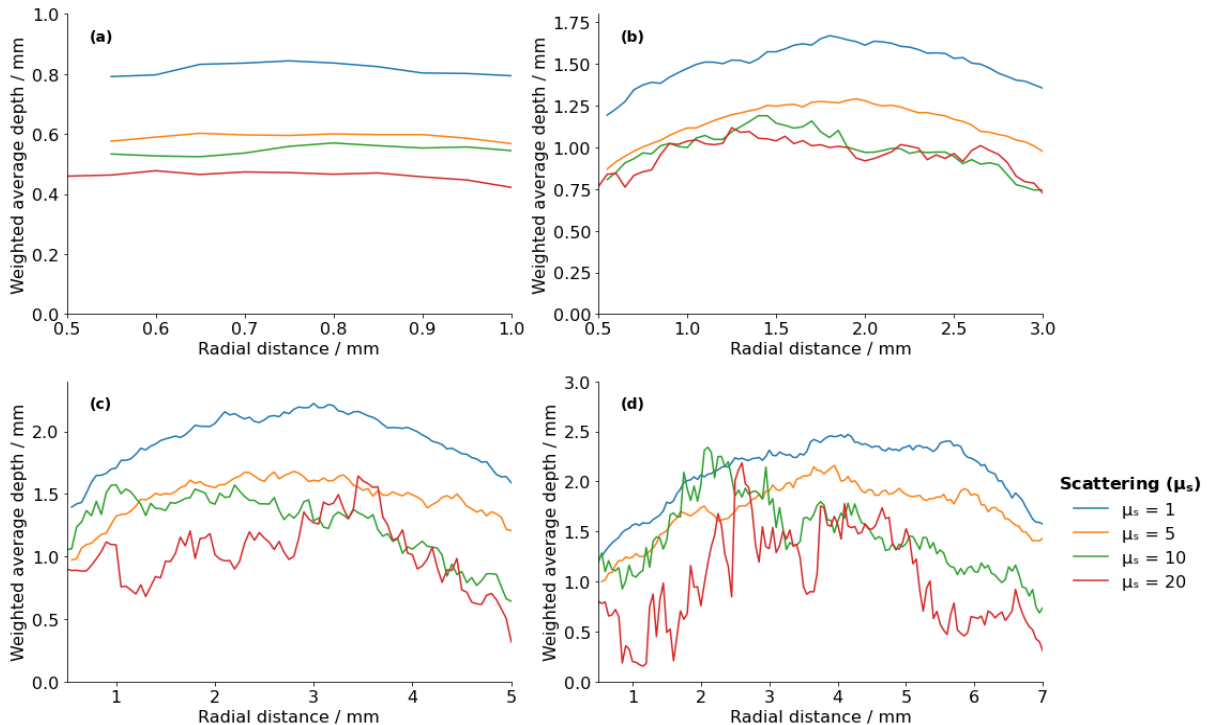
Figure 31: Simulated depth sensitivity profiles at fixed absorption ($\mu_a = 0.01$ mm^{-1}) and anisotropy ($g = 0$) for varying scattering coefficients (μ_s). The four subplots display how the average photon path changes for different μ_s values. The subplots correspond to fixed SDS of: (a) 1 mm, (b) 2 mm, (c) 3 mm, and (d) 4 mm.

Figure 31 reconfirmed that as μ_s decreases deeper and broader photon migration from the source photons is enabled. Conversely, increasing μ_s leads to shorter photon paths and more sensitivity, especially pronounced at larger source–detector separations. The sensitivity seen for the 20 mm^{-1} scattering coefficient could be due the small sample size of that bin due to the steep decrease in reflectance as the SDS increases.

The initial Monte Carlo simulations provided a crucial theoretical foundation, validating the expected relationships between optical properties, photon depth migration, and spatial reflectance patterns. By varying absorption, scattering, and anisotropy, the model established baseline behaviours against which experimental measurements could be compared. With this groundwork laid, attention turned to applying the Monte Carlo model to experimentally derived optical parameters. Using absorption (μ_a) and reduced scattering (μ'_s) coefficients obtained from curve-fitting the interactance data, new simulations were performed to predict depth sensitivity profiles for realistic tissue phantoms. These fitted-parameter simulations enabled a direct comparison between theory and experiment, providing a test of the model's predictive capabilities. The results of these simulations, along with their comparison to experimental reflectance and depth measurements, are presented in the Results and Discussion section.

References

1. P. W. Atkins, J. De Paula and J. Keeler, Atkins' Physical Chemistry, 12th edn, Oxford University Press, Oxford, 2023.
2. Introduction to Biomedical Optics, lecture slides, ECE 532, 3. Optical Properties, 2025.
3. R. A. J. Groenhuis, H. A. Ferwerda and J. J. T. Bosch, J. Opt. Soc. Am., 1983, 22, 2456–2462.

4. C. C. Johnson, IEEE Trans. Biomed. Eng., 1970, 17, 129–133.

5. K. M. Case and P. F. Zweifel, Linear Transport Theory, Addison-Wesley, Reading, Mass., 1967.

6. L. Reynolds, C. Johnson and A. Ishimaru, Appl. Opt., 1976, 15, 2059–2067.

7. A. Ishimaru, Wave Propagation and Scattering in Random Media, Academic Press, New York, 1978.

8. L. G. Henyey and J. L. Greenstein, Astrophys. J., 1941, 93, 70–83.

9. L. Reynolds, J. Molcho, C. Johnson and A. Ishimaru, Optical Cross Sections of Human Erythrocytes, Alliance for Engineering in Medicine and Biology, Washington, 1974.

10. W. G. Egan and T. W. Hilgeman, Optical Properties of Inhomogeneous Materials, Academic Press, New York, 1979.

11. R. A. J. Groenhuis, H. A. Ferwerda and J. J. T. Bosch, J. Opt. Soc. Am., 1983, 22, 2462–2472.

12. D. Spitzer and J. J. Ten Bosch, Appl. Opt., 1975, 17, 129–137.

13. P. S. Mudgett and L. W. Richards, Appl. Opt., 1971, 10, 1485–1502.

14. P. S. Mudgett and L. W. Richards, Appl. Opt., 1972, 11, 551–567.

15. W. E. Meador and W. R. Weaver, Appl. Opt., 1979, 18, 1204–1208.

16. M. Keijzer, W. M. Star and P. R. M. Storchi, Appl. Opt., 1988, 27, 1820–1824.

17. T. J. Farrell, M. S. Patterson and B. Wilson, Med. Phys., 1992, 19, 879–888.

18. J. D. Moulton, Diffusion Modeling of Picosecond Laser Pulse Propagation in Turbid Media, MSc thesis, McMaster University, Ontario, Canada, 1990.

19. R. C. Haskell, L. O. Svaasand, T. T. Tsay, T. Feng, M. S. McAdams and B. J. Tromberg, J. Opt. Soc. Am. A, 1994, 11, 2727–2741.

20. A. K. Kienle and M. S. Patterson, J. Opt. Soc. Am. A, 1997, 14, 246–254.

21. Z. Wang, Y. Yin, Z. Shan, Q. Cui, W. Zhang, B. Chai, D. Li, Z. Yu and B. Su, Herit. Sci., 2024, 12, 51.

22. X. Ye, T. Doi, O. Arakawa and S. Zhang, Sci. Rep., 2021, 11, 21982.

23. F. A. Kruse, A. B. Lefkoff, J. W. Boardman, K. B. Heidebrecht, A. T. Shapiro, P. J. Barloon and A. F. Goetz, Remote Sens. Environ., 1993, 44, 145–163.

24. K. H. Norris, NIR News, 2005, 16(8), 10–13, Why log(1 / R) for composition analysis with NIR.

25. Pigments Gums and Resins, Blue Verditer Pigment, available at: https://www.kremer-pigmente.com/en/shop/pigments/10180-blue-verditer.html (accessed April 2025).

26. Kremer Pigmente, Blue Bice Pigment, available at: https://www.kremer-pigmente.com/en/shop/pigments/10184-blue-bice.html (accessed April 2025).

27. C. Schmidt, P. Casadio, E. Price, J. Mass and K. Trentelman, Heritage Science, 2024, 12, 63. DOI: 10.1038/s40494-024-01257-7.

28. Sigma-Aldrich, Rose Madder (Alizarin), Dye Content 97%, CAS Number 72-48-0, available at: https://www.sigmaaldrich.com (accessed April 2025).

29. Royal Society of Chemistry, Carmine Red, $C_{22}H_{20}O_{13}$, available via ChemSpider, https://www.chemspider.com (accessed April 2025).

Appendix

1.
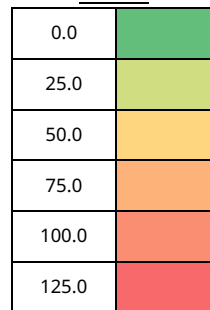
Table 7: Data matrix showing the SAM scores for the comparison of every pigment samples' log (1/R) spectra.

	Krem. Bone black	Corn. Lamp black	Ald. Prussian blue	Corn. Antwerp blue	Guado (WOAD)	Maya blue	Corn. Lapiz L	Corn. Egyptian blue	Krem. Blue bice	Krem. Blue verditer	Corn. Blue verditer	Corn. Azurite
Krem. Bone black	0.0	1.8	10.6	16.5	38.4	35.2	30.6	15.1	20.3	18.7	15.5	19.7
Corn. Lamp black	1.8	0.0	10.0	15.9	39.4	36.1	31.3	15.0	20.5	18.8	15.6	19.8
Ald. Prussian blue	10.6	10.0	0.0	7.0	39.0	34.3	28.3	8.4	15.5	13.1	10.0	14.7
Corn. Antwerp blue	16.5	15.9	7.0	0.0	41.8	36.5	31.5	10.5	14.5	12.0	10.2	13.7
Guado (WOAD)	38.4	39.4	39.0	41.8	0.0	9.3	19.1	35.6	35.6	37.1	37.1	36.0
Maya blue	35.2	36.1	34.3	36.5	9.3	0.0	15.5	29.6	29.6	31.3	31.8	30.2
Corn. Lapiz L	30.6	31.3	28.3	31.5	19.1	15.5	0.0	23.6	27.0	27.6	27.3	27.2
Corn. Egyptian blue	15.1	15.0	8.4	10.5	35.6	29.6	23.6	0.0	10.9	9.4	7.7	10.5
Krem. Blue bice	20.3	20.5	15.5	14.5	35.6	29.6	27.0	10.9	0.0	3.1	6.1	1.5
Krem. Blue verditer	18.7	18.8	13.1	12.0	37.1	31.3	27.6	9.4	3.1	0.0	3.5	2.3
Corn. Blue verditer	15.5	15.6	10.0	10.2	37.1	31.8	27.3	7.7	6.1	3.5	0.0	5.2
Corn. Azurite	19.7	19.8	14.7	13.7	36.0	30.2	27.2	10.5	1.5	2.3	5.2	0.0
Corn. Smalt light	43.0	43.6	40.3	42.8	19.9	18.7	16.2	36.3	40.0	40.7	40.5	40.1
"lev." azurite	17.9	18.1	12.9	12.4	36.3	30.8	27.0	9.5	3.5	1.8	3.2	2.4
Krem. Ultramarine ash	14.0	15.2	17.5	22.6	25.4	22.8	19.1	16.0	19.1	19.2	17.3	19.0
Corn. Verdigris	24.5	23.9	17.6	12.1	46.8	40.5	38.6	17.8	16.0	14.7	15.2	15.9
Krem. Fib malachite	16.0	15.6	17.7	18.5	47.5	42.7	40.3	19.4	18.4	17.2	15.9	18.1
Corn. Terre verte	29.0	30.3	34.4	38.7	20.8	21.4	26.2	31.8	31.1	32.5	31.9	31.5
Corn. Yellow ochre	43.2	44.4	52.2	56.9	42.5	46.0	49.8	52.1	50.7	51.7	50.5	50.9
Krem. Yellow ochre	38.7	39.9	47.5	52.5	38.3	41.8	44.5	47.4	46.5	47.3	46.1	46.6
Corn. Rose madder	48.6	49.7	54.3	59.5	35.4	42.6	41.6	54.4	55.4	56.0	54.6	55.2
Corn. Carmine red	45.5	46.8	51.3	56.5	32.5	39.5	38.4	51.3	52.3	52.9	51.5	52.1
Corn. Red ochre	30.5	31.9	38.0	43.5	30.1	34.2	33.4	38.7	39.4	39.8	38.1	39.2
Krem. Red ochre	28.9	30.3	36.5	41.9	29.3	33.0	32.2	37.0	37.8	38.2	36.4	37.6
Mars red	31.3	32.6	39.1	44.5	31.2	35.4	34.9	39.8	40.6	40.9	39.2	40.4
Krem. Brown Ochre	25.3	26.6	33.2	38.7	29.9	32.6	31.6	33.9	34.9	35.2	33.4	34.7
Corn. Gypsum	17.5	18.8	25.4	30.4	31.5	31.6	30.6	26.5	27.0	27.1	25.2	26.8
Corn. Marble dust	7.9	9.3	15.7	21.2	33.1	31.2	27.8	18.0	20.9	20.2	17.5	20.4
Kaolinite	64.1	65.3	71.4	75.1	53.9	57.1	62.6	68.6	64.1	66.1	66.3	64.6
MgCO$_3$	73.4	72.1	69.6	67.5	103.8	98.2	90.6	73.5	78.2	75.8	74.7	77.5
TiO$_2$	77.5	78.2	82.4	84.4	72.6	72.4	77.1	78.1	72.0	74.0	75.2	72.8
Zinc white	72.8	73.5	77.2	79.0	69.8	69.0	73.2	73.0	67.1	69.1	70.4	67.7
Salt (NaCl)	12.8	11.7	7.7	10.5	44.0	39.9	33.6	15.3	22.4	19.8	16.9	21.5

	Corn Smalt light	lev." azurite	Krem Ultramarine ash	Corn Verdigris	Krem Fib malachite	Corn Terre verte	Corn. Yellow ochre	Krem. Yellow ochre	Corn. Rose madder	Corn. Carmine red	Corn. Red ochre	Krem. Red ochre
Krem. Bone black	43.0	17.9	14.0	24.5	16.0	29.0	43.2	38.7	48.6	45.5	30.5	28.9
Corn. Lamp black	43.6	18.1	15.2	23.9	15.6	30.3	44.4	39.9	49.7	46.8	31.9	30.3
Ald Prussian blue	40.3	12.9	17.5	17.6	17.7	34.4	52.2	47.5	54.3	51.3	38.0	36.5
Corn. Antwerp blue	42.8	12.4	22.6	12.1	18.5	38.7	56.9	52.5	59.5	56.5	43.5	41.9
Guado (WOAD)	19.9	36.3	25.4	46.8	47.5	20.8	42.5	38.3	35.4	32.5	30.1	29.3
Maya blue	18.7	30.8	22.8	40.5	42.7	21.4	46.0	41.8	42.6	39.5	34.2	33.0
Corn. Lapiz L	16.2	27.0	19.1	38.6	40.3	26.2	49.8	44.5	41.6	38.4	33.4	32.2
Corn. Egyptian blue	36.3	9.5	16.0	17.8	19.4	31.8	52.1	47.4	54.4	51.3	38.7	37.0
Krem. Blue bice	40.0	3.5	19.1	16.0	18.4	31.1	50.7	46.5	55.4	52.3	39.4	37.8
Krem. Blue verditer	40.7	1.8	19.2	14.7	17.2	32.5	51.7	47.3	56.0	52.9	39.8	38.2
Corn. Blue verditer	40.5	3.2	17.3	15.2	15.9	31.9	50.5	46.1	54.6	51.5	38.1	36.4
Corn. Azurite	40.1	2.4	19.0	15.9	18.1	31.5	50.9	46.6	55.2	52.1	39.2	37.6
Corn. Smalt light	0.0	40.2	32.2	49.7	53.6	35.3	57.6	52.9	43.4	41.6	41.7	41.1
lev. azurite	40.2	0.0	18.1	16.0	17.3	31.5	50.5	46.1	54.4	51.4	38.3	36.7
Krem. Ultramarine ash	32.2	18.1	0.0	29.8	24.8	17.7	38.1	33.0	40.4	36.9	23.5	21.7
Corn. Verdigris	49.7	16.0	29.8	0.0	18.0	42.6	60.1	56.6	68.1	64.8	50.6	48.8
Krem. Fib malachite	53.6	17.3	24.8	18.0	0.0	35.7	47.3	44.1	60.3	57.2	40.7	39.0
Corn. Terre verte	35.3	31.5	17.7	42.6	35.7	0.0	25.6	21.4	34.6	30.6	18.6	16.7
Corn. Yellow ochre	57.6	50.5	38.1	60.1	47.3	25.6	0.0	6.0	6.0	31.5	21.9	21.7
Krem. Yellow ochre	52.9	46.1	33.0	56.6	44.1	21.4	6.0	0.0	30.3	27.4	16.2	16.0
Corn. Rose madder	43.4	54.4	40.4	68.1	60.3	34.6	6.0	30.3	0.0	6.7	21.8	23.7
Corn. Carmine red	41.6	51.4	36.9	64.8	57.2	30.6	31.5	27.4	6.7	0.0	18.3	20.0
Corn. Red ochre	41.7	38.3	23.5	50.6	40.7	18.6	21.9	16.2	21.8	18.3	0.0	2.5
Krem. Red ochre	41.1	36.7	21.7	48.8	39.0	16.7	21.7	16.0	23.7	20.0	2.5	0.0
Mars red	43.0	39.4	24.6	51.5	41.3	19.1	20.5	14.9	22.0	18.6	1.9	3.2
Krem. Brown Ochre	41.3	33.8	18.9	45.5	35.3	16.1	22.7	17.0	26.9	23.4	5.9	4.0
Corn. Gypsum	42.5	25.8	13.5	36.2	25.9	16.7	27.5	22.7	36.4	32.9	15.8	14.0
Corn. Marble dust	40.3	19.0	9.4	28.6	19.9	22.4	37.0	32.2	42.3	39.0	23.5	21.8
Kaolinite	68.5	65.0	56.7	75.9	64.2	41.9	28.5	31.3	45.2	44.4	43.1	43.3
MgCO3	95.2	76.5	85.1	67.2	69.8	100.4	108.2	105.7	110.9	110.2	99.6	98.7
TiO2	83.9	73.6	72.6	81.4	71.2	61.8	53.2	55.6	70.2	69.6	66.7	66.4
Zinc white	80.0	68.6	68.7	76.7	66.8	59.7	54.4	55.8	67.9	67.7	64.7	64.3
Salt (NaCl)	44.1	19.6	22.8	20.8	20.4	39.5	55.3	50.7	56.6	53.9	40.9	39.5

	Mars red	Krem. Brown Ochre	Corn. Gypsum	Corn. Marble dust	Kaolinite	MgCO3	TiO2	Zinc white	Salt (NaCl)
Krem. Bone black	31.3	25.3	17.5	7.9	64.1	73.4	77.5	72.8	12.8
Corn. Lamp black	32.6	26.6	18.8	9.3	65.3	72.1	78.2	73.5	11.7
Ald Prussian blue	39.1	33.2	25.4	15.7	71.4	69.6	82.4	77.2	7.7
Corn. Antwerp blue	44.5	38.7	30.4	21.2	75.1	67.5	84.4	79.0	10.5
Guado (WOAD)	31.2	29.9	31.5	33.1	53.9	103.8	72.6	69.8	44.0
Maya blue	35.4	32.6	31.6	31.2	57.1	98.2	72.4	69.0	39.9
Corn. Lapiz L	34.9	31.6	30.6	27.8	62.6	90.6	77.1	73.2	33.6
Corn. Egyptian blue	39.8	33.9	26.5	18.0	68.6	73.5	78.1	73.0	15.3
Krem. Blue bice	40.6	34.9	27.0	20.9	64.1	78.2	72.0	67.1	22.4
Krem. Blue verditer	40.9	35.2	27.1	20.2	66.1	75.8	74.0	69.1	19.8
Corn. Blue verditer	39.2	33.4	25.2	17.5	66.3	74.7	75.2	70.4	16.9
Corn. Azurite	40.4	34.7	26.8	20.4	64.6	77.5	72.8	67.7	21.5
Corn. Smalt light	43.0	41.3	42.5	40.3	68.5	95.2	83.9	80.0	44.1
lev. azurite	39.4	33.8	25.8	19.0	65.0	76.5	73.6	68.6	19.6
Krem. Ultramarine ash	24.6	18.9	13.5	9.4	56.7	85.1	72.6	68.7	22.8
Corn. Verdigris	51.5	45.5	36.2	28.6	75.9	67.2	81.4	76.7	20.8
Krem. Fib malachite	41.3	35.3	25.9	19.9	64.2	69.8	71.2	66.8	20.4
Corn. Terre verte	19.1	16.1	16.7	22.4	41.9	100.4	61.8	59.7	39.5
Corn. Yellow ochre	20.5	22.7	27.5	37.0	28.5	108.2	53.2	54.4	55.3
Krem. Yellow ochre	14.9	17.0	22.7	32.2	31.3	105.7	55.6	55.8	50.7
Corn. Rose madder	22.0	26.9	36.4	42.3	45.2	110.9	70.2	67.9	56.6
Corn. Carmine red	18.6	23.4	32.9	39.0	44.4	110.2	69.6	67.7	53.9
Corn. Red ochre	1.9	5.9	15.8	23.5	43.1	99.6	66.7	64.7	40.9
Krem. Red ochre	3.2	4.0	14.0	21.8	43.3	98.7	66.4	64.3	39.5
Mars red	0.0	6.4	16.3	24.4	42.3	100.0	66.3	64.4	41.8
Krem. Brown Ochre	6.4	0.0	10.6	18.3	44.8	95.6	66.7	64.3	36.3
Corn. Gypsum	16.3	10.6	0.0	10.2	49.2	88.5	68.1	65.1	28.7
Corn. Marble dust	24.4	18.3	10.2	0.0	57.9	80.5	74.0	69.8	19.0
Kaolinite	42.3	44.8	49.2	57.9	0.0	124.0	34.0	36.4	76.0
MgCO3	100.0	95.6	88.5	80.5	124.0	0.0	116.1	110.0	64.0
TiO2	66.3	66.7	68.1	74.0	34.0	116.1	0.0	20.5	87.6
Zinc white	64.4	64.3	65.1	69.8	36.4	110.0	20.5	0.0	82.0
Salt (NaCl)	41.8	36.3	28.7	19.0	76.0	64.0	87.6	82.0	0.0

Scale

0.0	
25.0	
50.0	
75.0	
100.0	
125.0	

2.

Table 8: A data table of SAM score obtained from interpolating and comparing visible and FORS spectra for the same pigment.

	pigment	SAM	
		rad	degrees
Blues	Ald Prussian blue	0.08	4.40
	Guado (WOAD)	0.04	2.37
	Maya blue	0.02	1.35
	lev. azurite	0.01	0.84
	Krem. Blue bice	0.02	0.97
	Krem. Blue verditer	0.02	1.04
	Krem. Ultramarine ash	0.03	1.53
	Corn. Antwerp blue	0.06	3.21
	Corn. Azurite	0.03	1.88
	Corn. Blue verditer	0.02	1.23
	Corn. Smalt light	0.03	1.97
	Corn. Egytian blue	0.03	1.88
	Corn. Lapiz L	0.03	1.70
Greens	Corn. Verdigris	0.03	1.65
	Corn. Terre verte	0.02	1.20
	Krem. Fib malachite	0.03	1.64
Yellows	Krem. Yellow ochre	0.06	3.44
	Corn. Yellow ochre	0.05	3.09
Reds	Corn. Carmine red	0.05	2.73
	Corn. Red ochre	0.04	2.05
	Corn. Rose madder	0.04	2.05
	Mars red	0.04	2.48
	Krem. Red ochre	0.03	1.87
	Krem. Brown Ochre	0.04	2.24
Blacks	Krem. Bone black	0.04	2.07
	Corn. Lamp black	0.03	1.83
Whites	Corn. Gypsum	0.21	11.76
	Corn. Marble dust	0.19	10.64
	Kaolinite	0.25	14.20
	MgCO3	1.68	96.38
	TiO2	0.36	20.88
	Zinc white	0.78	44.63
	Salt	0.30	17.08

Scale

0	
5	
25	
50	
75	
100	